Development of a Novel Microwave Sensing System for Lab on a Chip Applications

by

Shinong Mao

A thesis
presented to the University of Waterloo
in fulfillment of the
thesis requirement for the degree of
Master of Applied Science
in
Mechanical Engineering

Waterloo, Ontario, Canada, 2018

AUTHOR'S DECLARATION

I hereby declare that I am the sole author of this thesis. This is a true copy of the thesis, including any required final revisions, as accepted by my examiners.

I understand that my thesis may be made electronically available to the public.

Abstract

Microwave technology presents tremendous potential as a remote-sensing technology for a wide range of applications spanning from life science research to food industries, pharmaceutical research, and new material discoveries. Integration of microwave sensing with microfluidics for sample processing makes it an ideal choice for point of care applications highly demanded in resource-limited areas. The vast majority of the existing microwave sensors are manufactured using sophisticated soft lithography technology which has largely limited its development and applications. There is a large demand for developing new fabrication approaches for the feasibility of mass production at a reasonable cost.

In this thesis, a new, yet simple method is developed to fabricate split ring resonator (SRR) based microwave sensors. A simple RLC model is used to characterize the resonant frequency of the SRR, and the equations for calculating the RLC's resonant frequency is modified to predict the SRR's resonant frequency base on its geometry. The design is also validated by comparing the simulation results obtained using the commercial software HFSS, and measurements from a real SRR developed sensor. The double ring structure was fabricated onto a printed circuit board by using the industrial photolithograph method. Coating with PDMS and epoxy layer as the passivation layer was tested and compared.

Two testing approaches using the SRR sensor developed in this thesis are implemented in this thesis. Their performance for real-time sensing is characterized by applying it to differentiate chemical diary samples and other chemical solutions. In the dipping mode, the sensor is dipped in the material under test (MUT), and in the microfluidic channel mode, the sensor is integrated with a microchannel. The MUT is characterized by analyzing the spectrum data of the reflection coefficient as the function of frequencies. Experimental results indicate that this sensor is capable of differentiating various liquid samples such as DI water, ethanol, isopropanol, oil and salt solutions. Linear relationships between the resonant frequency and the concentrations of chemical composites are also observed in ethanol solutions (0-90%), and salt solutions (NaCl). This sensor is also used to differentiate various milk samples and milk dilutions and it is capable of distinguishing milks with different fat percentages and protein contents.

A fully customized vector network analyzer (VNA) is also developed. The circuit structure is designed by referring the existing customized VNAs that were implemented in previous work by other lab colleagues. Modifications are made including replacement of the microwave source, using Arduino platform to perform controlling and data acquisition, addition of a harmonic filtering device, and development of a calibration algorithm. The device is validated by comparing its measuring result with a commercial VNA. The customized VNA is able to output a similar spectrum pattern as the commercial VNA, but with slightly shift of the peak frequency.

Acknowledgements

First of all, I would like to I would like to express my very great appreciation to my supervisor, Dr. Carolyn Ren, for giving me this precious opportunity to work under the guidance with her valuable and constructive suggestions during the planning and development of this research work. Also, I would like to thank Dr. Ning Qin for his great help at the beginning stage of my research.

Next, I would like to thank Dr. Fei Chen, who is the CEO of QuantWave technologies for his generous support and help. I would also like to thank the colleagues of the QuantWave who provide helps on my research, Luqi Chui, Dr. Yin Li.

I also want to thank Qihang Wu for his suggestions and helps on my programming.

I would also thank all the members of the Waterloo Microfluidics Laboratory, without whom my master study life would not have been so colorful.

Finally, I would like to thank to my family: my parents and my grandparents for their encouragement, support and love.

Table of Contents

List of Figures

List of Tables

Nomenclature

BOM	Bill of Material
CMOS	Complementary Metal-oxide-semiconductor
DAQ	Data Acquisition
DI	Deionized
DUT	Device under Test
IDEs	Insulated Interdigital Electrodes
LOC	Lab on a Chip
µTAS	micro-Total Analysis System
PCB	Print Circuit Board
PDMS	Polydimethylsiloxane
PLL	Phase Loop Lock
IQ	In-phase and Quadrature
RF	Radio Frequency
SMA	SubMiniature Version A
SRR	Split Ring Resonator
USB	Universal Serial Bus
VCO	Voltage Control Oscillator
VNA	Vector Network Analyzer

Chapter 1

Introduction

1.1 Background

The idea of Lab-on-a-chip (LOC), which is also known as micro-Total Analysis System (µTAS), is proposed to miniaturize and integrate multiple chemical and biological processes onto a tiny device (Chow, 2002).That concept could be well illustrated in Figure 1.1. There are a lot of advantages of using this miniaturized system, such as lower sample and reagent consumption, greater control of reactions, higher sensitivity and throughput, and lower cost. Therefore, as the result of its massive advantages, the LOC technology has attracted growing attention by academic researchers and industries on its potential applications on nanobiotechnology, medicine development and material science.

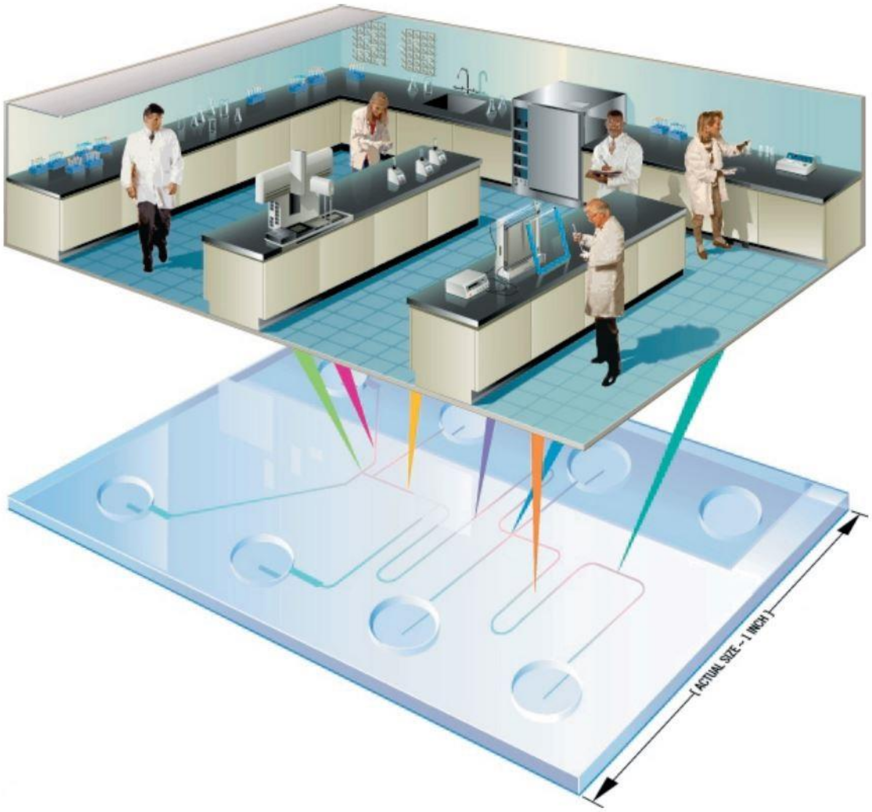

Figure 1-1 Schematic diagram of integrating a conventional macroscale laboratory onto a microscale chip (Chow, 2002)

A classic LOC platform generally contains a network of microfluidic channels and other components. Liquid samples could be manipulated inside the channel, such as dilution, concentration, filtration, labelling and separation etc. The system can achieve on-chip sensing and detecting with the help of electronic or optical sensors. The fully integrated and automated system has great potentials on point-of-care applications. Nowadays, most of the microfluidic components are fabricated from the master, which is a silicon wafer with photo resistant mold on it, by soft lithography technique. It is a good technique for fast prototyping, but there are still some challenges that limits its development on practical applications.

Resonator-based microwave sensing is a compromising technology which could be integrated with microfluidic devices for achieving on-chip sensing and detection. A microwave sensor usually applies its surrounding electromagnetic fields to sense the dielectric properties of the substance existing within the field region. Planar resonator, which is an offshoot of the microwave resonators, can achieve a contact free, label free on-chip sensing and detection of high sensitivity and rapid response. Different types of planar resonators such as transmission line resonators, split ring resonators (SRRs) have been developed and well-studied in the previous research. These sensors reveal great potentials in the applications of sensing and detecting liquids contents in the microchannel.

Though LOC systems have been developed for over 20 years and the mechanisms of the flow manipulations and sensing techniques have also been well researched, only a few of those academic achievements could be successfully transformed into practical applications because of their supplicated and expensive fabrication processes. Therefore, it is necessary to keep searching for novel fabrication methods to solve these issues with the aim of transforming more ideas of LOC from academics to industries.

.

1.2 Objective of This Thesis

Several PDMS microfluidic chips combined with glass-based SRR sensor have been developed previously, for sensing or heating of liquids in micro scale (Boybay, Jiao, Glawdel, & Ren, 2013; Yesiloz, Boybay, & Ren, 2015) The systems are able to distinguish different liquids such as oil, DI water, salt solutions and glucose solutions. They are also capable of measuring the liquid temperature within microfluidic channels (Wong, Yesiloz, Boybay, & Ren, 2016). However, the fabrication of glass-based SRR sensor, which is the core component on those chips for sensing and heating, usually requires photolithography and electrical plating processes which are sophisticated, time consuming and expensive. The quality of the sensor could not be well controlled through manufacturing process, which might lead to high failure rate and low consistency among different sensors. Bonding of PDMS channels and the glass-based sensor is also complicated due to using plasma treatment, and misalignment of the channel with sensor occurs with high probability. Furthermore, the PDMS material might also be easily contaminated because its porous structure may trap small molecules (Toepke & Beebe, 2006). Therefore, the LOC system that applies PDMS microfluidic channels combing with glass-based SRR sensor does not satisfy the requirements for mass production of practical applications.

Vector Network Analyzer (VNA) has become a common electrical measuring equipment to characterize the response of a passive component versus frequency or measure the impedance. Though the VNA technology has been developed over decades, it is still an expensive and bulky device. The VNA might also have a slow response which could not meet the requirements for high throughout measurements. Moreover, VNA hardware and software are usually not open source, so it could not be customized for specific applications. Several customized VNA circuits were proposed, developed and implemented in recent years for decreasing the cost and size, increasing the measuring speed and gaining greater control on operations (Martinez, 2012; Mcdermott & Ireland, 2004; Yesiloz et al., 2015). However, those systems are still complex and expensive for developing commercial application, because the system are not fully customized with either commercial RF synthesizer or Data Acquisition (DAQ) equipment used.

The objectives of this thesis are as follows:

1. Redesign, optimize the geometries of the Split-Ring-Resonator (SRR) sensor.
2. Develop a new fabrication process for single-port SRR sensors that is feasible for mass production with affordable costs.
3. Propose a simplified theory to interpret the response of the SRR sensor.
4. Propose and implement emailer detection and measuring approaches using the new developing sensors.
5. Evaluate the performance of different detection methods.
6. Propose and develop a fully customized VNA circuit.

1.3 Thesis Outline

Chapter 2 reviews microfluidic technologies combined with sensing techniques and their applications. Various sensing approaches for microfluidics are overviewed. The rational needs for microwave sensing are addressed. Basic principles of dielectric measurement with microwave sensing are explained and various measuring techniques are summarized and discussed. Microwave measuring principles and techniques are also presented, by introducing the concept of the scattering parameters and the vector network analyzer.

Chapter 3 begins with the interpretation of the working mechanism of SRR by the series RLC circuit theory. A PCB-based SRR sensor is designed and developed followed by a 3-stage process, as the calculations of the SRR frequency with modified equations, numerical simulation of the response of the structure and sensor validation by measurements of the real sensor. Fabrication of sensor trace and coating of the passivation layer are also presented. Frequency from the 3 stages are compared at the end.

In chapter 4, two testing methods by using the PCB sensor made from chapter 3 are presented. It begins with the dip-mode testing followed by the tape-channel-mode approach. Details of the fabrication of sensor form each mode are presented. Their experimental setup and procedures are also illustrated. The testing results of both methods are interpreted, compared and discussed. Errors and uncertainty sources are also discussed for each testing approach.

In chapter 5, structures of the customized VNAs that were developed on previous work are reviewed. Limitations and challenges of those solutions are summarized, which is followed by the plans for the improvements. A fully-customized VNA structure is then proposed and implemented. Details of each components are presented.

In chapter 6, the contributions of this thesis are summarized, and recommendations for future works are also provided. The recommendations focus on improvements on calculation formulas and simulation models for more accurate prediction of the resonant frequency of SRR as well as the improvements on VNA design and fabrication for decreasing the noises and increasing the stability of the measurements.

Chapter 2 Literature Review

This chapter starts with the overviews of the existing sensing and detection techniques for microfluidic applications. The advantages and limitations of each sensing method are compared, and the needs for exploring microwave sensing approaches are discussed. This is followed by the introduction of the basic working principles of various microwave sensing techniques as well as their advantages and disadvantages. The applications of resonator-based microwave sensors are also reviewed. This is followed by introducing the design approaches of a microwave sensor. Finally, a review of microwave measuring techniques and measurement equipment is also provided.

2.1 Sensing Techniques for Microfluidics

Sensing and detection of liquid contents in microfluidics are two of the most important features of the LOC applications. The LOC may lose its advantages of high integration, short reaction time and the small volume of reagent consumptions if the treated sample is not able to be characterized onsite. A variety of techniques have been developed integrating with the microfluidics to detect the sample within the channels. They can be classified into three main categories as optical methods, electrochemical approaches, and mass spectrometry techniques (Wu & Gu, 2011). Optical and electrical methods are the most widely applied in microfluidic sensing applications because of their flexibility, high sensitivity, and capability of selective sensing. Several optical and electrical methods that are widely used in microfluidics will be reviewed in this section, and the rational needs for microwave sensing will also be discussed.

2.1.1 Optical Methods

Optical measurement is one of the most basic techniques to inspect and monitor the operations and reactions on microfluidic systems. Generally, an optical measurement system for microfluidics consists of a microscope and a camera or specific light sensing devices. The materials under test are typically measured directly with a camera or indirectly by their optical responses under specific lights. Indicators might be required to label the specific substance for selective measurements. Four typical optical measurement approaches and their working principles are summarized and demonstrated in figure 2.1.

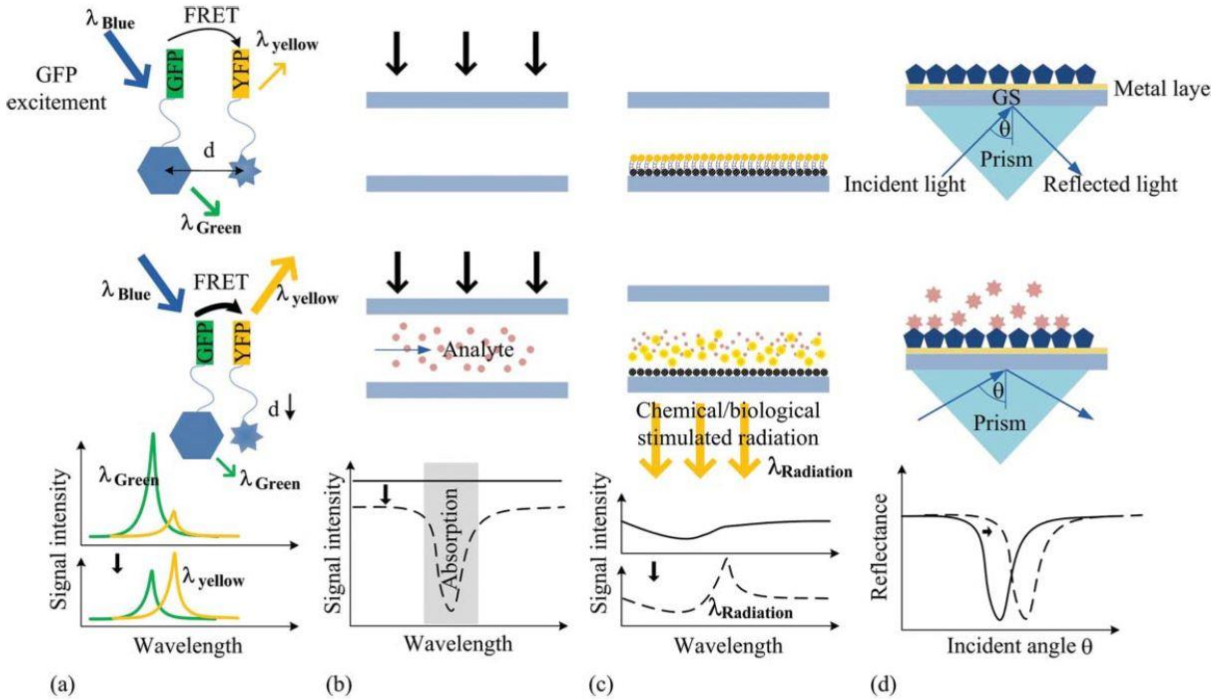

Figure 2-1 Summary of 4 conventional optical detection methods based on (a) fluorescence method, (b) absorbance method, (c) luminescence method and (d) surface plasmon resonance-based optical detection methods ((Wu & Gu, 2011).

2.1.2 Electrical Methods

Electrical approaches can also be used with microfluidics for sensing and detecting purpose. The property of the liquid could be characterized by measuring the impedance and capacitance information which are determined by the sample contents. Capacitance could be measured in microscale by multiple types of probes. A capacity sensor with a pair of electrodes that forms the gap laying underneath the channel was developed for liquid discrimination and characterization (Demori, Ferrari, Poesio, & Strazza, 2011). Insulated interdigital electrodes (IDEs) were also implemented for detecting the existence of droplets (Dong & Barbosa, 2015). The gaps of the IDEs are aligned vertically under the channel, so they can detect the existence, size and the even flow speed of a droplet. Chen et al. (2004) made a 1-dimensional array of capacitance electrode under the channel for droplet positioning and volume measuring inside the microchannel. The electrode array could be expanded to 2 detention on a PCB board for both position detection and content sensing (Medoro et al., 2003). The 2-dimensional array could be further miniaturized and integrated onto a CMOS chip (Medoro, Guerrieri, Manaresi, Nastruzzi, & Gambari, 2007). The capacitance measurement approach is simple, stable and affordable, but it usually has a low specificity of sensing. Impedance methods were also used in previous research. A cell-based biosensor was developed for testing the toxicity of drinking water on a LOC platform (Curtis et al., 2009). The impedance of the biosensor is determined by the toxicity, so they can monitor the drinking water by tracking the impedance of the sensor.

2.1.3 Rational Needs of Microwave Sensing

Though optical and electrical sensing techniques have been well developed and some of them are widely applied in numerous practical applications, they still have disadvantages and limitations while being integrated with microfluidics. Optical sensing techniques usually require huge, sophisticated and expensive equipment, which makes it challenging for LOC applications. Fluorescent chemicals are usually used for detecting the specific substance, which may raise the cost and bring potential contaminations. Electrical sensing method might not be sensitive and rapid enough for high throughput detections. Therefore, it is necessary to combine a new detection approach that can be integrated into LOC applications and perform label-free detections with a rapid response. Microwave sensing techniques operate at radio frequency (RF) range, which increases the detection sensitivity and response speed. A label-free and non-contact sensing can also be achieved by microwave sensing because it senses with electric and magnetic fields which can penetrate several millimeters into the tested samples. Microwave sensing also has better sensing performance on bio cells compared with the low-frequency measuring techniques (Gawad et al., 2004). For those reasons, the microwave could be a better sensing approach to be integrated with the microfluidics. Several common microwave sensing techniques and their applications are summarized as follows.

2.2 Review of Microwave Sensing Techniques

In this section, basic principles and some common microwave sensing methods will be summarized. Applications of the resonator-based microwave sensors on microfluidics will also be overviewed.

2.2.1 Dielectric Constant and Its Measurement Methods

Dielectric constant is defined as the ratio of the permittivity of a material to the permittivity of the free space. It also indicates the ability of the energy storage of a material when there is an external electric field applied onto it. It is the unique physical property of a specific substance. Therefore, a substance could be characterized by measuring its unique dielectric constant.

The dielectric constant could be measured by multiple approaches such as the coaxial probe method, the transmission line method, the free space method, and the resonant cavity method. Their working mechanisms, measuring parameters and characteristics are summarized as table 2.2 (Jabita & Abiodun, 2013). Those methods could be broken into two main categories depending on whether a resonator is used. The benefits and challenges of the resonant methods and broadband methods are summarized as Table 2.3.

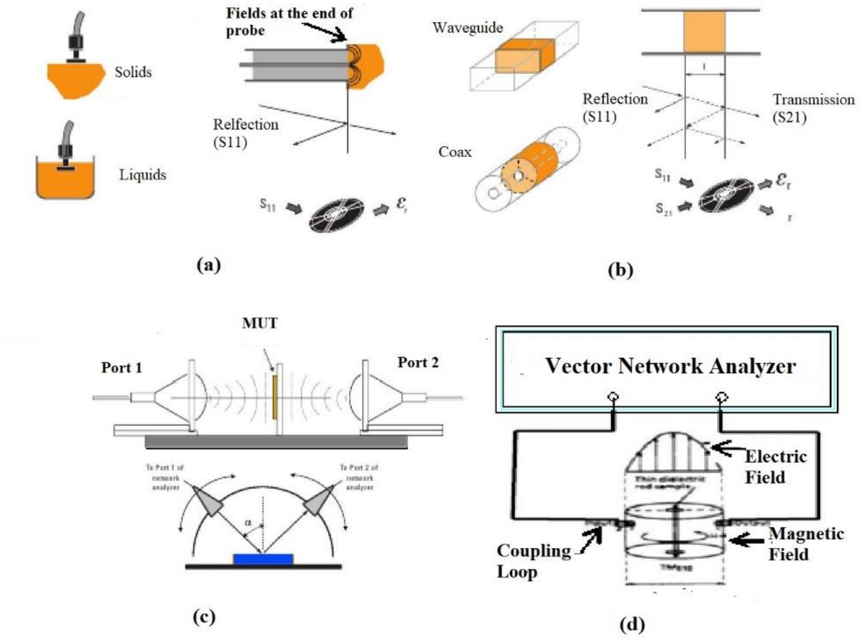

Figure 2-2 Summary of four common dielectric measurement methods: (a)coaxial probe method, (b) transmission line method, (c) free space method, d-resonant cavity method (Jabita & Abiodun, 2013).

Table 2-1 Summary of various dielectric measurement techniques

Methods	**Mechanisms**	**Measuring parameters**	**Response**	**Advantages**	**Limitations**
Coaxial probe	Electrical fields built at the end of the probe, relatively permeability, ε_r change within that region will alter the wave reflection	Reflection coefficient	Broadband spectrum	Broadband, simple, suite for liquids and semi-solids	Limited accuracy, requires a flat measuring surface
Transmission line	DUT is placed inside a waveguide, the wave reflection and transmission are determined by the ε_r of sample	Reflection coefficient & Transmission coefficient	Broadband spectrum	Broadband, can measure magnetic materials	Strict requirements of the shape and size of DUT, no air gap allowed
Free space	DUT is placed between a pair of TX and RX antennas, wave transmission and phase delay are determined by the ε_r	Reflection coefficient & Transmission coefficient	Broadband spectrum	No contacts with the sample, suitable for extreme environments	DUT has to be large enough
Resonant cavity	Insertion of the DUT into the cavity will alter the resonant frequency and quality factor, the extent of the shift is determined by ε_r	Resonant frequency & Quality factor	Narrowband peak	Can be miniaturized	Operates at a narrow bandwidth

Table 2-2 Comparison between the broadband and resonant approach

	Resonant methods	Broadband methods
Benefits	• Supports high impedance environment • Can be miniaturized, and low sample consumptions • Suitable for low loss materials	• Wide bandwidth, can measure at a broader frequency range • Gain more information
Limitations	• Narrow working bandwidth • Limited information acquired from the resonator	• Large and could not be miniaturized • Require a large amount of sample

2.2.2 Application of Planer Resonator-based Sensor in Microfluidics

As presented above, only the resonant method could be miniaturized down to the microscale, for integration with the microfluidic channels. However, the waveguide cavity resonators presented above are bulky and could not be integrated with microfluidic devices. Planer resonators, as another offshoot of microwave resonators, have attracted growing attention on integration with microfluidic devices and other remote sensing applications, because of its capability of miniaturization. The resonator is fabricated onto a specific substrate, and the microfluidic channel could be placed on the top of the resonator. Two types of the planer resonators were developed for microfluidics on previous studies which are a transmission line resonator and a split ring resonator (figure 2.3). The transmission line resonators also have various types such as the structure of three parallel aligned microstrips to monitor biological cells (Nikolic-Jaric et al., 2009), three microstrip arms that are aligned perpendicular with the transmission line for characterizing the complex permittivity (Chahadih et al., 2015), and the meander-line structure for quantitative monitoring of glucose (Chretiennot, Dubuc, & Grenier, 2016). There are more studies focusing on the implementations of SRR sensors on microfluidic applications because of its reduced size. In a SRR sensor, the resonant component and sensing structure are made together onto a ring. Glass-based with a single-gap SRR sensors were developed combining with the PDMS microfluidic channels for temperature sensing inside the channel (Wong et al., 2016) and characterization of the liquid contents with addition of a T-shape structures on the ring (Boybay et al., 2013) or spiral feature inside the gap (Yesiloz et al., 2015). Double-gap SRR sensor was also implemented with a capillary tube aligned within the two gaps for detecting various substances such as water, methanol, ethanol, and air (Abduljabar, Rowe, Porch, & Barrow, 2014). Single-ring-structure resonators were presented with the resonant structure placed between a pair of monopole antennas for glucose content sensing (Camli et al., 2016) or placed above a microstrip line for monitoring the concentration of sucrose, sorbitol, D-glucose and D-fructose (Harnsoongnoen & Wanthong, 2017). Square SRR sensors were also implemented for characterization of dielectric properties of liquids (Vélez, Su, Grenier, Dubuc, & Martín, 2017), and sensing the interface of oil sands (Mohammad Hossein Zarifi, Rahimi, Daneshmand, & Thundat, 2015). Selective sensing of molecular analytes by a SRR sensor was also achieved by the combination with Tio$_2$ nanotube arrays(M. H. Zarifi, Farsinezhad, Abdolrazzaghi, Daneshmand, & Shankar, 2016).

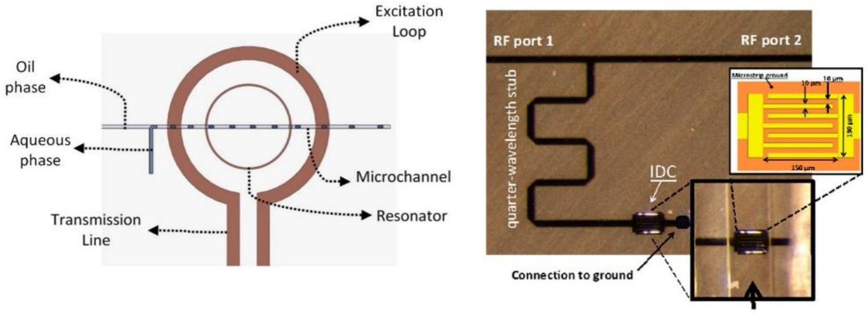

(a) (b)

Figure 2-3 Demonstration of: (a) a SRR sensor (Chretiennot et al., 2016) and (b) a microstrip line resonator (Boybay et al., 2013).

2.3 Design Approaches of SRRs

The development process of a SRR sensor usually has three stages as calculation from formulas, numerical simulation, and validation of the real component. This 3-stage design approach was implemented by Jabita (2013), for designing a SRR sensor. It starts with the mathematical analysis of the sensor following with the HFSS simulation. Finally, a real SRR sensor was made to evaluate the calculated and simulated results.

2.3.1 Calculations from Numerical Expressions

The physical parameters such as capacitance and inductance of a SRR are characterized as mathematical formulas by Sydoruk et al. (2009). The inductance of SRR was calculated by the numerical expression of a closed metal ring. The mathematical expressions of the capacitance of SRR were also derived. Those formulas were validated by Jabita (2013) by comparing the calculated and measured results, which matched well with each other. More details about the equations will be discussed in chapter 3.

2.3.2 Numerical Simulation

RF simulations are usually used for solving complex microwave problems such as solving S-parameters, electric current plot inside a conductor and radiation plot of an antenna. There are several choices of commercial RF simulation software that have been widely used in industries, such as HFSS, CST, and ADS. Among those, ADS does a better job on simulating circuits and RF components, and the other two software have better performances on antenna simulations. Different simulation techniques are used in HFSS and CST. The HFSS uses finite element method (FEM), whereas the CST applies the finite integration technique (FIT). However, the FEM has better performance for simulating antennas, and it can provide more details inside the 3D structures (Kozlov & Turner, 2010). Therefore, the HFSS is chosen to perform the simulation of the SRR design.

2.3.3 Experimental Validation of the SRR Sensor

The response of the SRR sensor versus frequency could be characterized by a VNA together with several different types coupling antennas. The sensor's spectral responses were characterized by placing it between a pair of monopole antennas and measuring the transmitting coefficients (Camli et al., 2016; Jabita & Abiodun, 2013). Another approach is to couple the wave to the SRR using a microstrip line (Harnsoongnoen & Wanthong, 2017). Double-ring structures were also applied, with the inner ring as a resonator and outer ring as excitation ring (Boybay et al., 2013; Yesiloz et al., 2015).

2.4 Vector Network Analysis of RF

In the RF field, the circuit or system are usually analyzed and interpreted by scattering matrix parameters. Multiple RF components are enclosed inside a closed block, and its overall incident, reflected and transmitted responses will be analyzed to simplify the complicated problems. An N-port network matrix is given in equation 2.1, where V_N^- is the incident wave’s voltage amplitude of port n and V_N^+ represents the amplitude of the reflected wave's voltage of the port n. The relations of the incident and reflected voltage of each port or between any two ports defined by the scattering matrix [S], which is interpreted as equation 2.2.

$$\begin{bmatrix} V_1^- \\ V_2^- \\ . \\ . \\ V_1^- \end{bmatrix} = \begin{bmatrix} S_{11} & S_{12} & \cdots & S_{1N} \\ S_{21} & & & \vdots \\ . & & & . \\ . & & & . \\ S_{N1} & \cdots & \cdots & S_{NN} \end{bmatrix} + \begin{bmatrix} V_1^+ \\ V_2^+ \\ . \\ . \\ V_N^+ \end{bmatrix} \tag{2.1}$$

$$S_{ij} = \frac{V_i^-}{V_j^+} \tag{2.2}$$

In this thesis, the SRR sensor is designed as a one-port component, and thus only S_{11} parameters are measured through all the tests. The S matrix of the one-port system is given as equation 2.3. The S_{11} represents the ratio of the amplitudes of the reflected wave over the incident wave, which is also known as the reflection coefficient.

$$S_{11} = \frac{V^-}{V^+} \tag{2.2}$$

VNA is a common RF measurement device for microwave network characterization that can measure the S-parameters of a RF component. VNAs usually have at least one port for measuring the reflection responses. Measurements of transmission parameters and even more complex S-parameters can be achieved by more than 2-ports. A VNA generally operates at a broad frequency range from several MHz up to tens or even 100 GHz. However, the cost of a VNA grows exponentially with the range of the frequency and number of the ports. Therefore, it is necessary to consider the working frequency range and the number of port while designing the microwave sensor.

2.4.1 Structure of Conventional VNA

A typical VNA consists of the microwave sources, direction couplers, gain detectors and data processing and interpretation systems. A simplified block diagram of a classic VNA structure is illustrated as figure 2.4. The wave from the variable frequency source is divided into two streams, with the REF1 for the incidence wave reference and the PC1 going to the device under test (DUT). A directional coupler can extract the reflected waves of DUT from the PC1 as TEST1. Waves from the local oscillator first mix with TEST1 and REF1 individually, and each mixed wave will be sampled by a high-speed sampler. That process is also known as QI modification and de-modification process by which the gain and phase of each stream can be computed. Finally, the ratio of the gain of the reflected wave over incident wave could be computed digitally.

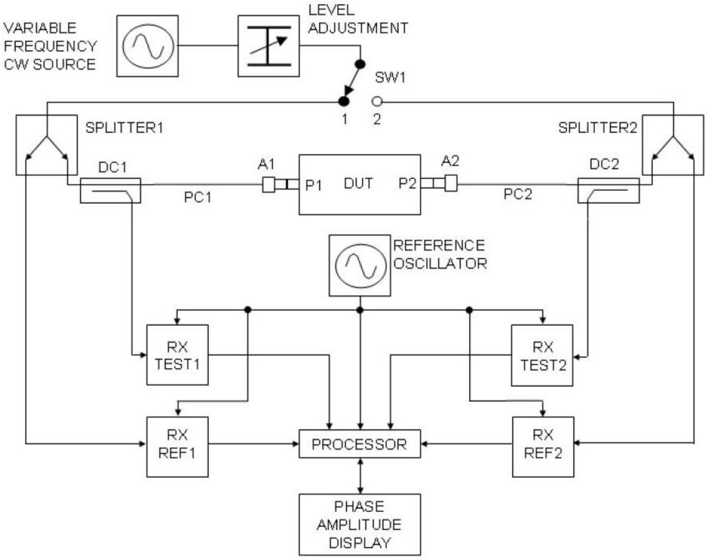

Figure 2-4 Structure of a typical VNA (Martinez, 2012).

2.4.2 Existing Customized VNAs

As illustrated above, a typical VNA has a complex structure which significantly increases the cost and size of the device and reduces the measuring speed due to the communications between multiple subsystems. Therefore, many attempts have been made for developing a more compact, more affordable and customized VNA. A simplified and low-cost VNA was developed by using a pair of directional couplers to individually extract incident and reflected wave and compare them by a gain and phase detector (Martinez, 2012). Another approach was to use a VCO as the wave source and bidirectional coupler to extract forward and backward waves (Yesiloz et al., 2015).

2.4.3 Calibration of the VNA

Same as other typical electric measurement equipment, VNA also requires calibration before performing tests. Errors are mainly caused by the imperfections of the directional coupler and the transmission line. A directional coupler only couples the wave from one direction in ideal situations, however it will receive waves from both directions in reality. As a result, the interference between the forward and backward coupled waves would contribute to the errors of the final results. The mismatch between transmission lines could cause the reflections and the standing waves that will also influence the measurement results. Those errors could be reduced by the proper calibration. Usually, a 3-term error model is used to recognize and quantitatively characterize the error sources from the transmission line as presented in figure 2.5. Three error factors are characterized from that model as directivity, port match, and tracking. They can be calculated from equation 2.3, with Γ as the real S11 and Γ as the measured S11. Thus, the three factors could be computed by measuring three know calibration kits which are a short, an open and a load kit.

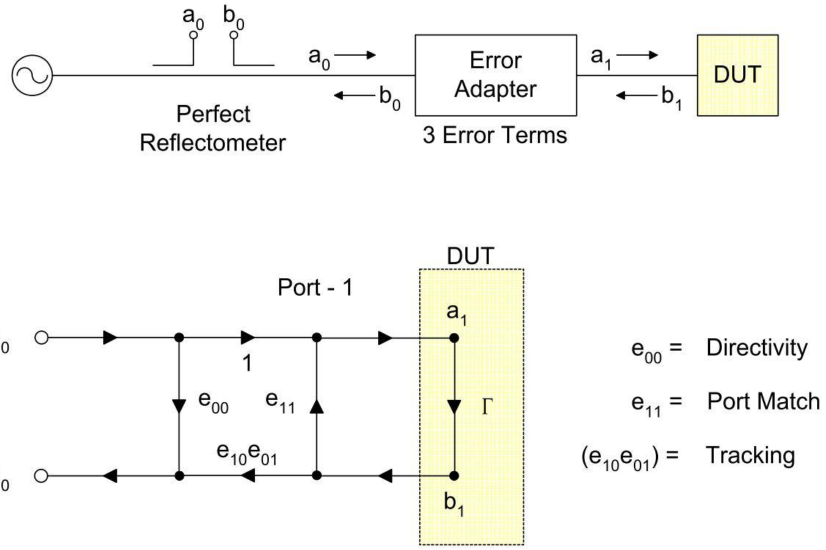

Figure 2-5 3-term error model of a one-port system (Rytting, 1998).

$$e_{11} + \Gamma\Gamma_M e_{11} - \Gamma\Delta e = \Gamma_M \qquad (2.3)$$

Chapter 3 Design, Optimization, and Fabrication of a PCB-based SRR Microwave Sensor

In this chapter, a SRR microwave sensor is developed on a print circuit board. The resonant frequency of the SRR is characterized by using the conventional series RLC circuit theory. Resonant frequency of a SRR is estimated by calculating the capacitance and the inductance of the ring resonator which are determined by its geometry. Various combinations of the design parameters are examined to optimize the ring resonator's resonant frequency. The ring resonator is also validated by high-frequency simulation software (HFSS). A PCB based SRR sensor was finally fabricated based on the optimized geometry.

3.1 Working Principles of a Ring Resonator

As discussed in chapter 2, the inner ring, which is working as a resonator, can be considered as a series RLC circuit. Therefore, its properties and performance can be analyzed using conventional electronic theories. The resonant frequency of the inner ring can be estimated by calculating its capacitance and inductance, and their numerical equation is expressed as equation 3.1. The resonant frequency f is

$$f = \frac{1}{2\pi\sqrt{LC}} \qquad (3.1)$$

The resonator's response of different samples can also be explained using RLC circuit model.
The capacitance and inductance of the ring resonator ar by its gap and copper trace respectively. Figure 3.1 shows the structure of a gap ring resonator and its simplified schematic diagram. Since the inductance is mainly determined by the copper trace itself, the ring resonator's response of the samples flowing above the gap is mostly dominated by the capacitance of the gap. If liquids with different dielectric properties exist within fringing field region of the gap, C_{gap} will change. As the result, the resonator's capacitance will change with different liquids. Therefore, the resonator's resonant frequency, resistance and quality factor will shift with various samples under test and reflected on the spectrum.

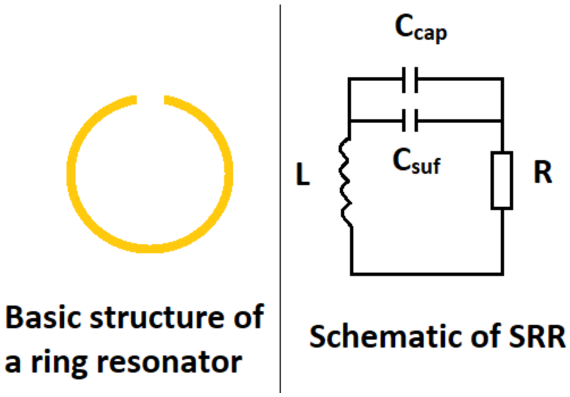

Figure 3-1 Structure of loop-gap-ring resonator (left side) and its electrical schematic (right side)

Ring-resonator-based microwave sensors can be broken into two main categories depending on the number of their ports. Figure 3.2 illustrates a single port sensor and a dual-port sensor, which were developed in previous research. Though similar loop-gap ring resonators are applied in both single-port and dual-port sensors, their working principles and measuring parameters are not the same. For one-port sensors, only reflecting properties are measured, whereas transmitting parameters are monitored in a dual-port sensor. In another word, in a single-port system, a VNA will detect the amount of the waves that are reflected from the sensor, and in a dual-port system, the VNA will estimate the portion of the waves that transmit from one port to another.

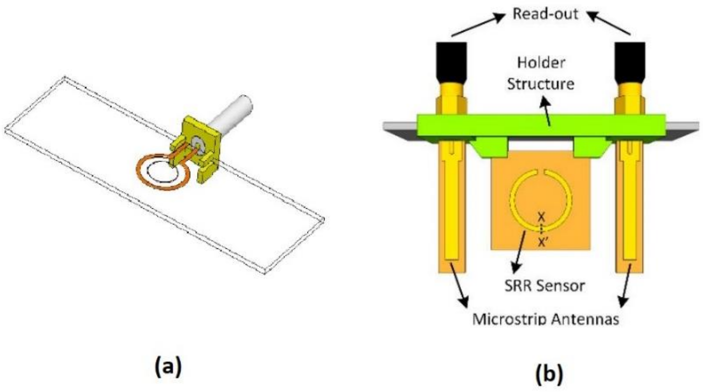

Figure 3-2 (a) single port SRR sensor developed onto a glass slide for microfluidic applications (Boybay et al., 2013), (b) dual-port SRR sensor operated with two monopole antennas (Camli et al., 2016).

The spectral response of the sensor is determined by the gap ring resonator's impedance as the function of frequency. The input impedance, Z of a series RLC circuit can be defined as the following equation(Pozar, 2012), and its spectrum versus frequency is interpreted in figure 3.3:

$$Z = R + j\omega \mathrm{L} - \mathrm{j}\frac{1}{\omega^2 LC} \qquad (3.2)$$

Notes: R: resistance
j : imaginary number
ω : angular frequency

A resonator tends to have less impedance around resonant frequency and its impedance reaches the lowest level at the resonant frequency. The impedance response can be reflected on the spectrum of the sensor on a VNA. Both single port and dual port sensor have a peak pattern at the resonant frequency on the spectrum. The ring resonator has the lowest impedance at its resonant frequency, and most of the wave will be coupled to the ring at that point. As a result, few waves could be reflected in a single port sensor or be transmitted to the receiving port in a dual port system. At other frequencies, most of the wave will be reflected to the port or transmitted to the other port. That explains the reason why the S_{11} reaches the lowest level at the resonant frequency forming a peak feature.

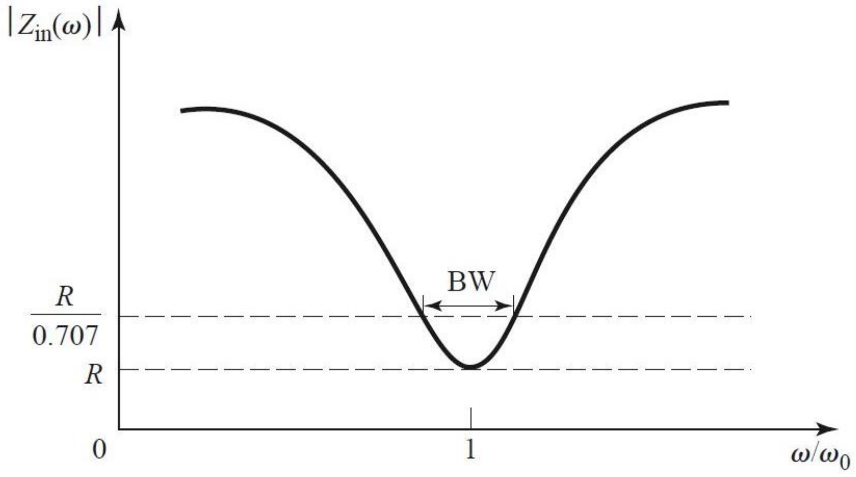

Figure 3-3 Input impedance versus frequency (Pozar, 2012).

A single port split ring resonator was adopted for designing the sensor. In this case, the sensor consists of 2 gapped rings as shown in figure 3.4. The outer ring is an excitation ring that connects directly to an SMA connector. The inner ring is a resonator whose resonating frequency is determined by the surrounding environments, especially the gap area.

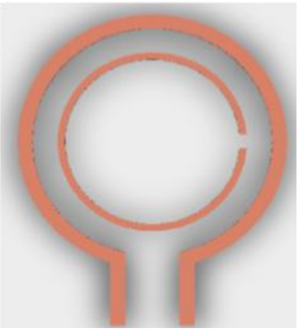

Figure 3-4 2D structure of the double SRR

3.2 Motivations of Developing a PCB-based Sensor

Glass-based SRR sensor combing with PDMS channels was successfully developed in the previous experiment studies (Yesiloz et al., 2015). The system is able to differentiate oil, ethanol, air and DI water that has large dielectric properties and it could also characterize the trends of KCl and ethanol solutions of gradient concentrations. The glass-based SRR sensor has many unique advantages. First, it is optically transparent which makes it an ideal option for combining with optical measurements such as droplet counting under the microscope. Second, the scale of the ring features can be as low as tens micrometers because the photolithographic technique is applied during the fabrication process. Third, the fabrication of PDMS microfluidic channels is a mature technology that makes it affordable, simple and rapid for various design in the prototyping stage. However, the glass-based sensor is not perfect. Its advantages could be the limitations while moving from research to the production stage. The challenges of developing the glass-based sensor are summarized as followings:

- High costs: The overall cost of a sensor can be divided into two parts which are BOM of the sensor and fabrication cost. Both of them are too high for making a real product. The majority cost of the BOM is from the copper-coated glass slides. The glass slide was coated with 5nm copper for electric plating. Usually, the copper film was sputtered onto the glass, which is a quite expensive process. The fabrication of the sensor is also expensive because it involves soft lithography and an electric plating process. Fabrication of the sensors also has a relatively high failure rate, which could also raise the cost.
- Not feasible for mass production: The fabrication of the glass-based senor is sophisticated due to lots of spin coating, UV exposing, electric plating and etching process involved. That would not be an issue for research purpose, but they are not practical for mass production because of the complex processes. Thus, the consistency and yield of the sensor could not be guaranteed.
- Short lifespan: The glass-based sensor may fail after 20-30 tests due to leakage or contaminations of the PDMS channel.

Therefore, new substrate materials and fabrication techniques need to be explored to reduce the cost and fabrication difficulties, which make it a more optimum for developing a product.

Printed circuit board, also known as the PCB, is the better option for making the sensor comparing with the glass slides. PCB has been developed for decades, and it is a mature technology and wildly applied in a wide range of electronic devices. Comparing with the glass-based sensor, PCB-based sensors have more consistencies in quality, lower cost and easier fabrication processes. Therefore, the SRR is redesigned, optimized and fabricated onto the PCB in this research.

3.3 Design and Optimization of the Sensor by Using RLC Theory

The capacitance and inductance of the resonator ring can be calculated by numerical equations. Previous research has investigated the relations between the geometry of a metal loop-gap ring and its resonant frequency(Jabita & Abiodun, 2013). A metal ring resonator was cut out from an aluminum block into the desired shape. A pair of monopole antennas and a two-port VNA were applied to characterize the ring resonator. The calculated frequency of the ring matched well with the testing result.

In this thesis, the equations for calculating the resonant frequency are modified because multiple dielectric substrates are introduced, which changes the response of the resonator. The PCB-based ring resonator is made onto an FR-4 substrate and coated with a film of passivation layer, whereas the metal ring resonator in the previous research had no substrate instead of air. Therefore, the dielectric coefficient of FR-4 and the passivation layer material need to be introduced into the equations while calculating the resonant frequency.

3.3.1 Calculating the Capacitance and Inductance of the PCB-based SRR

As discussed in chapter 2, the analytical expression of the capacitance and inductance of a metallic gap-ring resonator was proposed and experimentally exanimated on previous research (Sydoruk, Tatartschuk, Shamonina, & Solymar, 2009). The capacitance and inductance of the ring resonator are determined by its geometry, which are the inner radius of the ring, the thickness of the ring, the height of the ring, and the gap of the ring. In this study, the ring structure is made onto a piece of FR-4 board. The equations derived from the previous can still be used to characterize the PCB-based SRR, but several modifications are required on several parameters. The structure of the metal ring resonator from previous research and PCB-based SRR is illustrated in figure 3.5. The parameters that determine the capacitance, C and inductance, L are defined as the inner radius of the ring, R; the width of the trace, W; the thickness of the copper trace, T; the width of the gap, G.

The inductance of the gap ring can be characterized as a closed ring because the gap is much smaller comparing with the size of the ring. Its inductance can be approximated by the following equation(Grover, 1962):

$$L = \mu R'(ln\frac{8R\prime}{T+w} - 0.5) \qquad (3.2)$$

Note: µ is the effective permeability of the air and substrate

R' is the average radius of the ring, $R' = R + \frac{W}{2}$

The total capacitance of a SRR has two main parts, which are the gap capacitance and the surface capacitance. The gap capacitance can be calculated as the parallel plate capacitor equation. The fringing field effect is considered and added to the equation because the surface area of the parallel plate is small, and contribution of the fringing field capacitance cannot be neglected. The PCB-based sensor developed in this research is using the fringing field to sense the liquid sample. Thus, the gap capacitance, C1 is defined as equation 3.3 (Sydoruk et al., 2009).

$$C1 = \ \varepsilon[\frac{T+W}{G} + \frac{2\pi T}{\ln(\frac{2.4T}{W})}] \qquad (3.3)$$

Note: ε is the effective dielectric coefficient of the air and FR-4

The surface capacitance, C2 of the ring is contributed by its surface charge, and its expression can be approximated as equation 3.4 (Sydoruk et al., 2009):

$$C2 = \frac{2\varepsilon T}{\pi} ln\frac{4R}{G} \qquad (3.4)$$

Therefore, the total capacitance, C of SRR is:

$$C = C1 + C2 = \ \varepsilon\left[\frac{T+W}{G} + \frac{2\pi T}{\ln\left(\frac{2.4T}{W}\right)}\right] + \frac{2\varepsilon T}{\pi} ln\frac{4R}{G} \qquad (3.5)$$

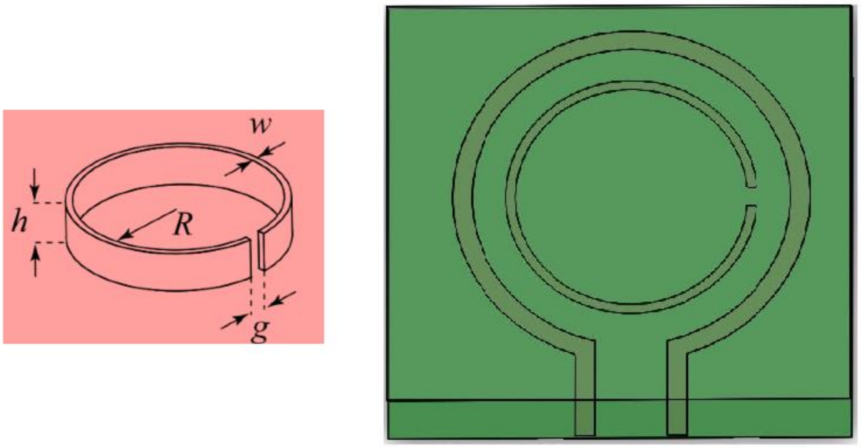

(a) (b)

Figure 3-5 Interpretation of the SRR structures: a- structure of metal ring (Jabita & Abiodun, 2013), b- structure of PCB-based SRR, with the inner ring as the resonator, the green board is the FR-4 substrate

3.3.2 Optimization of the Geometric Parameters

There are some restrictions while designing the ring resonator. First, the resonant frequency needs to be constrained within 2-3 GHz considering the significantly increased prices of the high frequency VNA's. At the higher operational frequencies, the requirement of the transmission line quality is stricter because the wavelength of the wave is comparable with the scale of the system. That will cause delays and interferences of waves within the transmission lines, and they contribute noises to the measurements. Second, the size of the gap and the width of the trace cannot be made as small as the micrometer scale due to the resolution limitations of the PCB fabrication techniques. Conventional PCB fabrication methods usually use milling method or etching method to create the copper trace. However, none of them are suitable for micrometer-scale trace fabrication. At that scale, the quality and consistencies of the sensors could not be guaranteed. Therefore, the geometry parameters of the ring need to be optimized to find the balance between the operational frequency and the fabrication resolutions.

The thickness of copper traces is determined by the type of the copper clad board, and it cannot be easily changed. In this thesis, the 1oz. Copper boards are used to manufacture the sensor. The thickness is approximately 0.036 mm. The gap width is finalized as 1 mm at the beginning because it has benefits for the channel-based sensor that will be discussed in chapter 4. The gap size of the new design is much wider than the glass-based one which is 200 µm. So the alignment between the channel and the gap is much simpler and more accurate. The larger size channel, as the result of the wide gap, could also reduce the fabrication difficulties and costs. Therefore, only radius and trace width values are optimized for calculating the resonant frequencies of different combinations of the R and W values. R values are from 4 to 8 mm with 0.1 mm step size. W values are from 0.1 to 1 mm with 0.05 step size. The resonant frequency is finalized at 2.7 GHz with W=0.5 mm and R = 6 mm. The final geometry parameters are listed in Table 3.1:

Table 3-1 Geometry parameters of the inner ring

Parameters	R	T	W	G
Values (mm)	6	0.036	0.5	1

The size of the outer ring does not significantly affect the response of the inner ring, because it operates as a short circuit instead of the resonator. But the spectrum of the double rings on VNA is also determined by the distance between the two rings because the coupling between the two rings is determined by their distance. The distance, D is kept the same as glass-based sensor design as 1.75 mm, which has been evaluated by earlier research (Boybay et al., 2013). So, the radius of the outer ring, R' = R+D. The width of the outer ring, W' is 1 mm and separation, S between the two soldering pins is 4.76 mm, to match with the width of pins on the SMA connector. The geometry parameters of the outer ring are summarized Table 3.2:

Table 3-2 Geometry parameters of the outer ring

Parameters	R’	W	T	S
Values (mm)	7.75	1	0.036	4.76

3.4 Simulation of the Design of SRR Sensor with Ansys HFSS

The parameters derived from the equations above are simulated by Ansys HFSS 15.0 version. A 3-dimentional object model of the PCB-based SRR is built first, and its resonant properties are characterized by simulating S21-parameters. In this thesis only the response of the inner ring is simulated with the HFSS for simplify the simulation.

The 3D module of the PCB is built following the parameters that are given in table 3.3, and it is illustrated in figure 3.6.

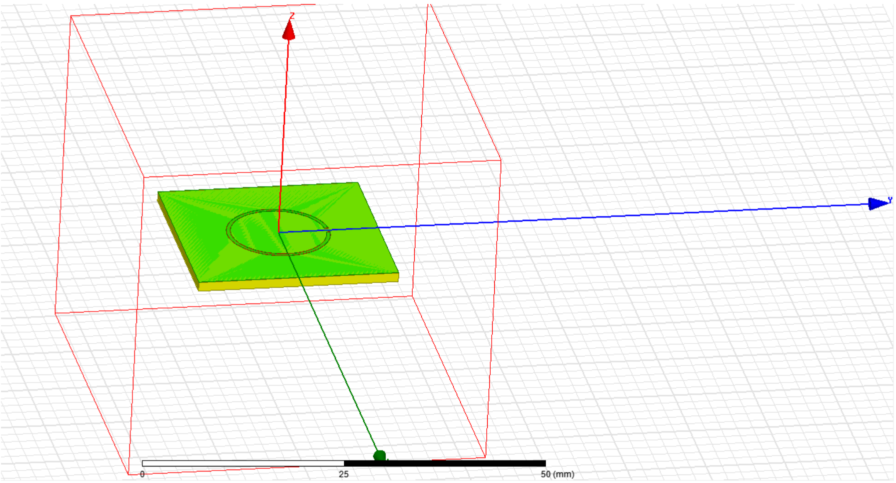

Figure 3-6 A 3D model built in HFSS

Table 3-3 Design parameters of the 3D modules for HFSS simulation

Object	Inner ring			Substrate board			Passivation layer		
Size (mm)	R = 6	W= 0.5	T= 0.036	L = 24	W= 24	T = 1	L = 24	W = 24	T = 0.041
Material	Copper			FR-4			Epoxy		

A cubic region that is defined as air is built surrounding the PCB sensor to create the background environment and boundaries for the simulations. It is mandatory because in HFSS, the default background environment is defined as a perfect electric conductor which is not the real condition. The size of the box is usually no less than a quarter of the operating wavelength.

Boundaries and excitation ports have to be first defined on the faces of the cubic region for performing the simulation. A pair of perfect boundaries are assigned to the two faces that are parallel to the XY plane, and a pair of PerfectE boundaries are assigned in the same manner to YZ faces as shown in figure 3.7.

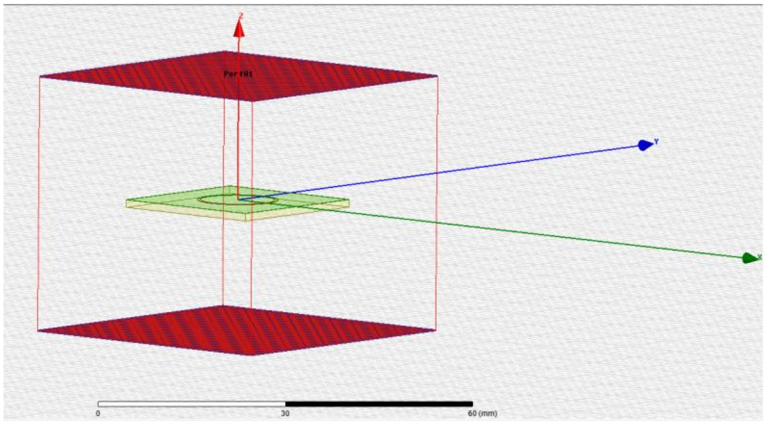

(a)

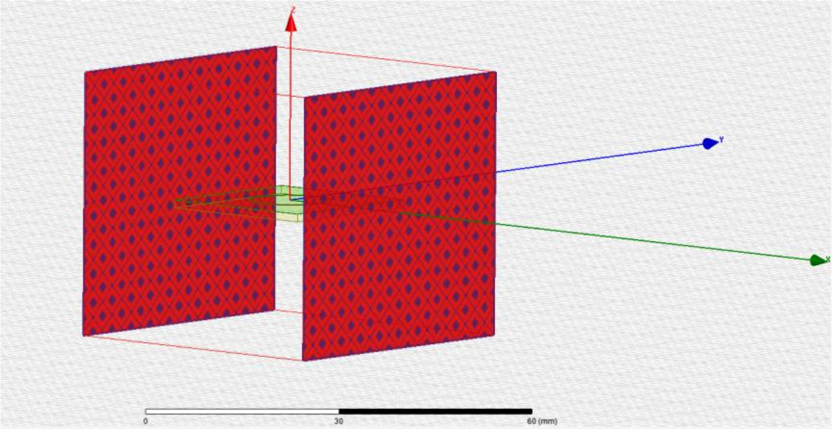

(b)

Figure 3-7 (a) assignment of PerfectH boundaries, (b) assignment of PerfectE boundaries.

Two excitation ports, with port1 for the wave entry and port2 for wave exit, are defined as the faces that are parallel with XZ plane. They are shown in figure 3.8.

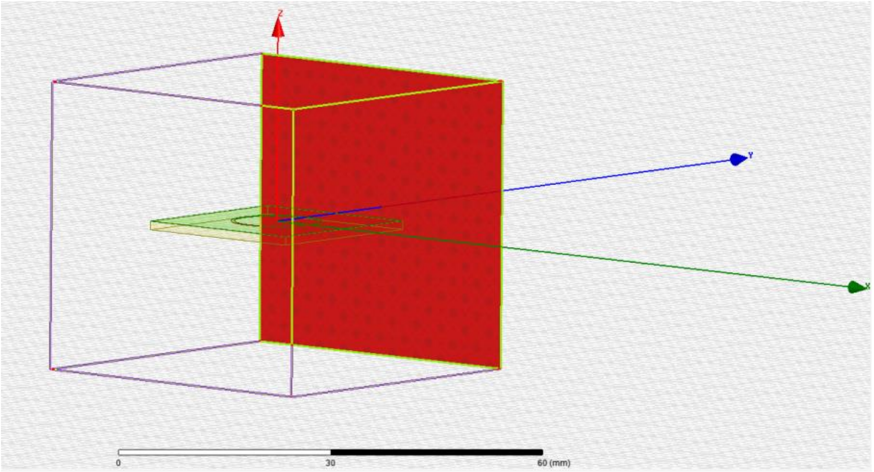

(a)

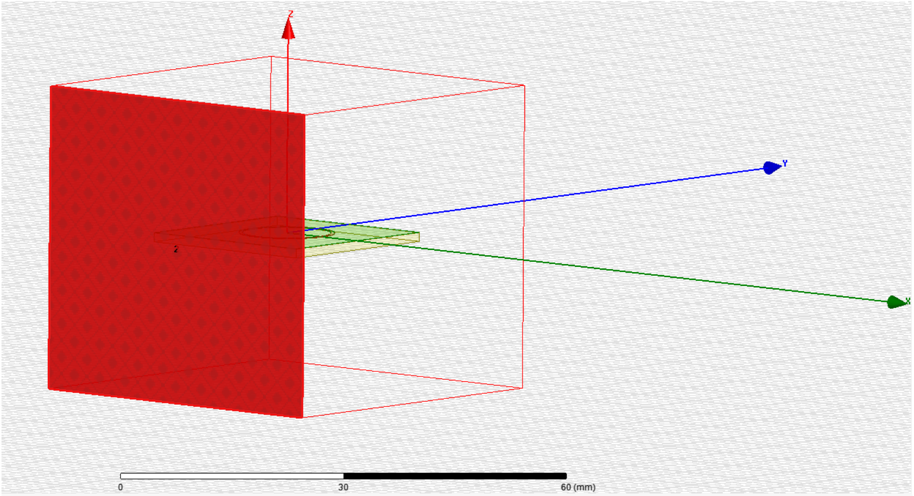

(b)

Figure 3-8 (a) assignment of wave entry port, (b) assignment of wave exit port

Therefore, the wave goes into port1 and propagates along y-axis within the cubic region where the SRR exists, and the wave will leave from port2. Driven Model is selected as the solution type for the simulation, which is usually used for predicting the resonant frequency of a 3D structure in HFSS. The frequency range is set from 1 to 4 GHz. The HFSS will perform the simulation after all the configuration parameters are properly defined. S12 results are exported in figure 3.9. The peak frequency locates at around 2.54 GHz.

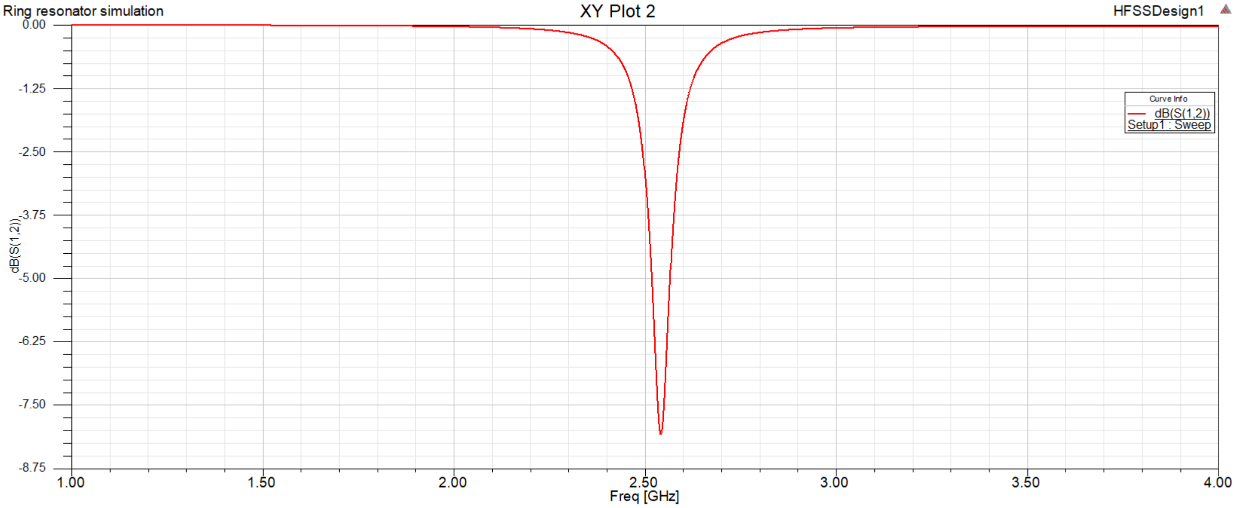

Figure 3-9 Plot of S21 from HFSS simulation of the PCB-based SRR, the peak frequency locates around 2.54 GHz.

3.5 Fabrication of the PCB-based Sensors

The sensor consists of two main parts which are a PCB with copper trace & FR-4 substrate and a thin passivation layer that isolates the copper trace from the liquid under test. The PCB circuit sensor is fabricated first, and then it is coated with the passivation layer.

3.5.1 Copper Trace Fabrication

Two common PCB fabrication techniques are applied in this experiment. The sensor is first produced by using a PCB milling machine (ProtoMat S103). The design file was imported to the machine, and a mill bit engraved the double-ring trace on a piece of single-side copper clad board, which is the only metal part remaining on the substrate. The mechanical machining method worked perfectly for the prototyping stage. Various designs could be turned into real boards in a short time and an affordable cost. However, the milling method is not able to achieve the high consistency requirements for different sensors, due to its low accuracy of the motion control and vibrations during machining processes. Therefore, the sensor fabrication was outsourced to an industrial PCB manufacture, which can provide sensors with higher quality, higher consistency. Figure 3.10 shows the comparison between two sensors that are fabricated with different methods.

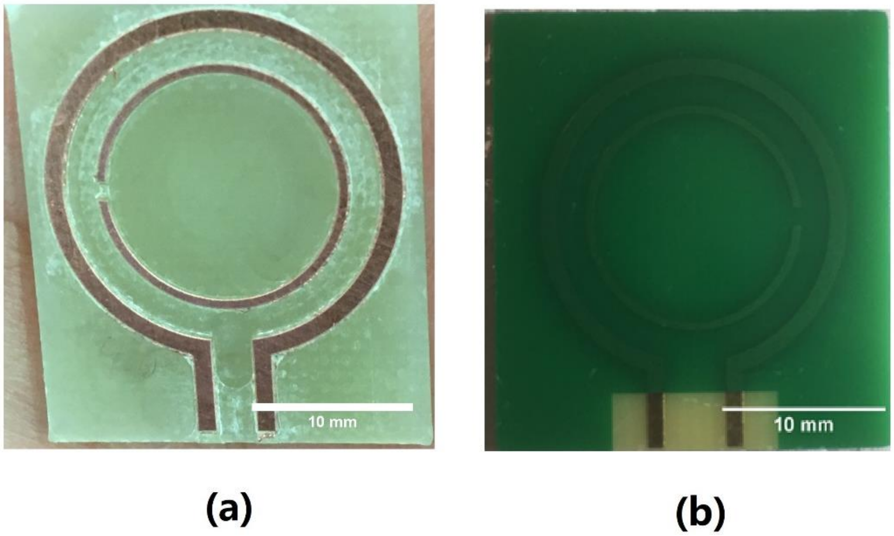

Figure 3-10 Comparison of the two sensors fabricated by (a) the milling method and (b) industrial manufacture.

3.5.2 Passivation Layer

A passivation layer is mandatory for the sensor for two main reasons. First, the sensor uses the fringing field to sense the liquid, which means that the liquid and copper should not contact with each other, so a film of electrical insulation layer has to be applied between them. Second, the exposed copper may also be easily oxidized by air. A protective layer needs to be covered onto the copper to prevent the copper trace from oxidization.

Two materials for making the passivation layer are evaluated during the fabrication processes. They are PDMS and epoxy polymer respectively. Finally, the epoxy polymer was chosen for making the passivation layer due to its advantages of the fabrication process and the material's properties.

The sensor is initially covered with a thin PDMS layer to form the passivation layer which isolates the copper trace with the tested liquids. For making the passivation layer, uncured PDMS mixture (with cure agent/ base mixed in 1:10 ratio by weight) is first treated under vacuum for ten minutes to remove bubbles, and the mixture was then gently poured onto the sensor's surface with the copper trace side facing upwards. The sensor is then placed onto the spinner for spin coating at 500 RPM for 1 minute. Finally, the sensor is cured by heating at 95 Celsius degrees for 12 hours.

The PDMS has many unique advantages such as the chemically inter properties and optical clearness, which make it a suitable material for producing microfluidics chips. The glass-based microfluidic sensors also applied a thin PDMS film as the passivation layer that separated the channel and copper sensor (Yesiloz et al., 2015). However, for PCB based sensors, this material has some weaknesses that make it not suitable for producing passivation layer. First, the PDMS could absorb and release small molecules from the solutions. Previous research revealed that the porous structure within the polymer might trap molecules and will affect the experiment result due to the absorption and release of those molecules (Toepke & Beebe, 2006). It can also be proved that there is a significant shift of the signal while dipping a dry the sensor into the DI water during the experimental tests in this thesis. The stabilization process might be caused by the absorption of H_2O molecules into the pores inside the PDMS. The absorption effect makes the PDMS act as a sponge, and it is hard to characterize the absorption and releasing process. Therefore, the real-time signal might reflect the combination of the sample under test as well as the absorbed substances, which make it inaccurate. Second, the thickness and homogeneity of the PDMS layer on the PCB surface cannot be well controlled. That is because that the surface of the PCB surface is not flat. The copper trace is about 0.035 mm higher than the substrate. It is not possible to generate a homogenous layer by using spin-coating, but the thickness of the coating is barely controllable without the spin-coating. Third, the PDMS material is too soft that shorten its lifespan. The PDMS based layer could be peeled off easily during cleaning after several tests. In summary, the PDMS is not a proper material for producing the passivation layer for the PCB sensors.

The epoxy polymer is a material that is wildly applied for making PCB solder mask, which could be used to replace the PDMS for making the passivation layer. It is an excellent electrical insulation material, and its uncured agent has a much lower viscosity, which makes it possible to spray onto the board to generate a much thinner layer. The solder mask coating is also a mature technology, which means that the quality of the coating is guaranteed by the industrial manufactures. In this case, the uncovered PCB sensors are sent to an industrial PCB fabrication foundry to coat the passivation layer. The epoxy polymer is sprayed onto the board to form a ten-micrometer layer. The stability of the sensor is significantly improved by using the epoxy layer. Therefore, all the experimental tests based on the PCB sensors in this thesis are conducted by the epoxy cover PCBs.

3.6 Experimental Measurement of the PCB-based SRR

The SRR sensor needs to be measured with a VNA to characterize its real response. The measurement results are also compared with the calculated and simulated results.

A single-port VNA that operates at the frequency range of 40 MHz to 4 GHz is used to measure the reflecting coefficients at each frequency, and they are interpreted as real-time spectrum plots. The VNA is calibrated with a short-open-load calibration kit before conducting any measurement. The sensor is directly connected to the VNA with a type N to SMA connector. Real-time peak frequency, which is also the resonant frequency of the inner ring resonator, is displayed on the VNA's graphical user interface as figure 3.10.

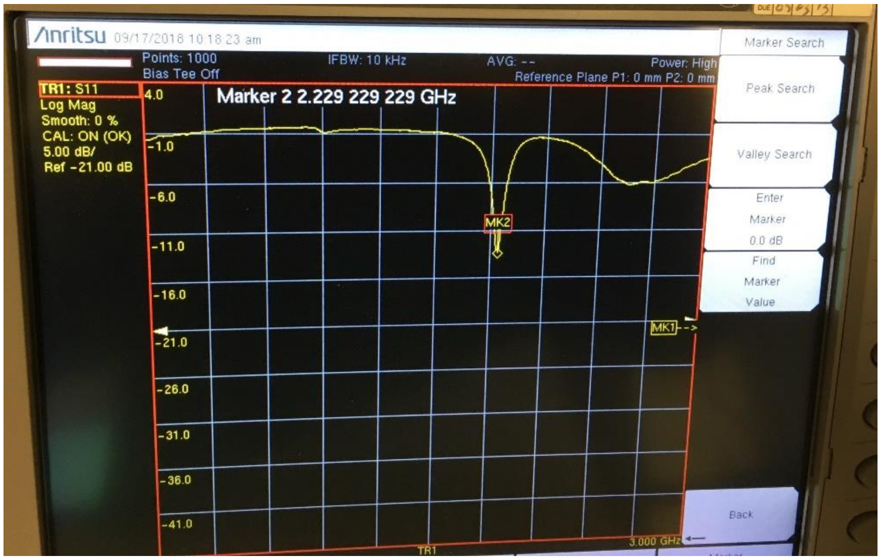

Figure 3-11 Measurement results of the PCB sensor with VNA

3.7 Results and Discussions

The resonant frequency results from the calculations from the derived equations, simulations by the HFSS software, and the experimental measurements from the VNA are given in the following table.

Table 3-4 Resonant frequency results of calculated, simulated and measured of the SRR

Analytical methods	Calculation	Simulation	Measurement
Resonant frequency (GHz)	2.7	2.54	2.23
Offset (GHz)	0.47	0.31	

Both calculated and simulated frequency results are slightly different from the actual resonant frequency of the SRR. The calculation results correspond more closely to the simulation results. The variance between the measured and estimated result might be caused by the existence of the outer ring. Both analytical equations and simulation model only character the single SRR instead of the double rings. The interaction between the inner and outer ring may influence the response of the resonator. The model might need to be optimized in future works to predict the resonant frequency more accurately.

Chapter 4 Development of Two Operating Modes of the PCB-based Microwave Sensor

In this chapter, two testing methods were developed by using the PCB sensors from the chapter3. Initial tests are performed for each testing modes to evaluate their abilities to distinguish different liquid samples such as DI water, ethanol solutions, and salt solutions. The effects of dielectric properties and ionic conductivities of the solutions are also studied by testing ethanol and NaCl solutions respectively with gradient concentrations. The uncertainty and error sources of each testing mode are discussed as well.

4.1 Dip-mode Sensor

Dipping mode is first proposed during this thesis by simply submerge the sensor vertically into the liquid. The response of the sensor is determined by the dielectric properties of the tested liquid sample. A testing system is also built and optimized to achieve a better testing performance.

4.1.1 Overview of the Dip-mode Sensor

The working principles of the dip-mode sensors are slightly different from the traditional SRR sensors, such as glass-based microfluidic sensor in the last chapter. The response of the dip-mode sensor is determined by not only the inner ring resonator but also the outer excitation ring as well as the interaction between the two rings. If the sensor is dipped into the liquid, the inductance of the copper ring will change compared with the air; the capacitances of the inner ring's gap and the gap between the two rings will also alter; the transmission efficiency from the excitation ring to the inner ring will also be affected. All those factors determine the spectrum response of a dipping mode sensor. The schematic of the dip-mode sensor could be implemented as figure 4.1. Both two rings are submerged into the liquid, as the result, the spectrum as well the peak are determined by 7 variables that are capacitance of the inner ring, $C_{innergap}$, resistance of the inner ring, R_{inner}, inductance of the inner ring,, capacitance of the outer ring, $C_{outer\ gap}$, resistance of the outer ring, R_{outer}, inductance of the outer ring, L_{outer}, and coupling coefficients between the two rings.

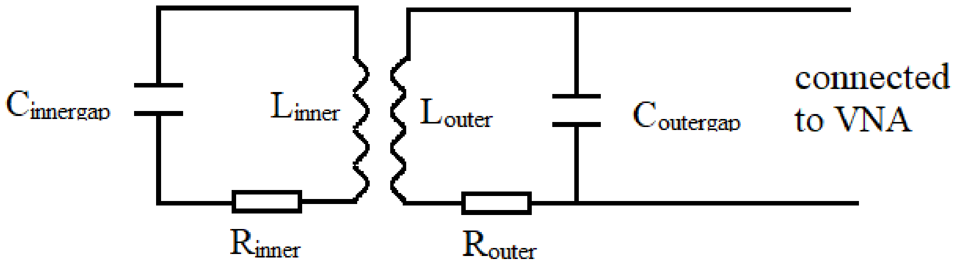

Figure 4-1 Electrical schematic diagram of double SRR.

4.1.2 Fabrication of the Dip-mode Sensor and Reservoir

The sensor system consists of two main components which are a PCB sensor with a cap as well as a reservoir that holds the liquid sample. They are made separately, and each component has multiple generations for the optimum performance and stability.

A cap is used with the dip-mode sensors for two main reasons. First, the cap can fix the PCB sensor and make it vertically oriented while being submerged into the liquid. Second, the cap can ensure that the PCB sensor is dipped at the same depth during each test. Thus, the cap can help reduce the operational uncertainties.

The cap is a 25.4 *25.4*3 mm board with a 23 * 1.5 mm opening in the center. The PCB sensor is inserted into the opening, and they are fixed using hot glue. The cap was first made by using 3D printers. 2 arm structures are also added to the 3D printed caps to protect the sensor and fix the position of the sensor while dipping into the reservoir. However, the 3D printed parts have coarse surfaces which are hard to clean and can be easily contaminated. Thus, the newer version of the cap is then developed with the opening laser cut from a 3mm thick acrylic board. The arm structures are also removed to avoid cross contaminations in that version. Hot glue is still used to fix the sensor onto the cap.

A customized sample reservoir is also designed and fabricated. It is a 25.4 mm cubic box with 1 mm thick wall. The reservoir is also made by 3D prints at the beginning. It is then changed to acrylic-board-assembled box because of the contamination issues of 3D printed parts. Therefore, the reservoir is finally made of glass by a glassware company, and it works perfectly through all the tests. Different generations of sensors with cap and reservoir are shown in figure 4.2.

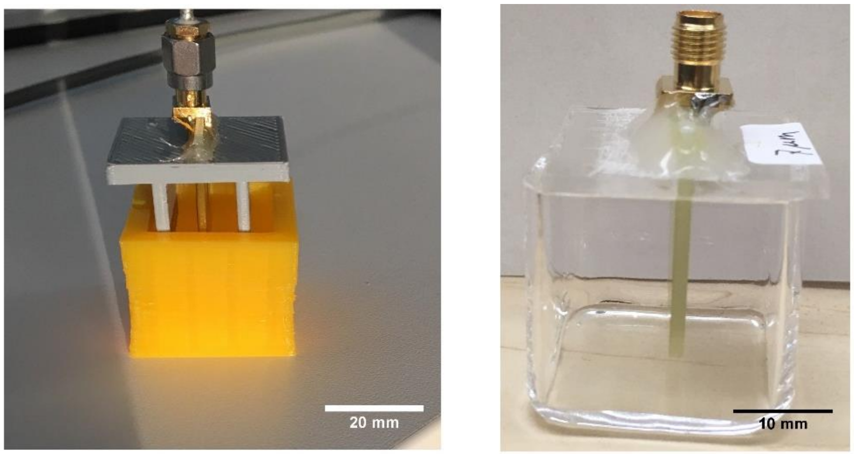

(a) (b)

Figure 4-2 Sensors and reservoirs of different version: a- 3D printed cap with arms and 3D printed sample holding box, b- laser cut cap with glass reservoir.

4.1.3 Testing with the Dip-mode Sensor

A testing system and its test procedures are developed for the dip-mode sensor. A one-port commercial VNA (Anritsu, MS46121B) is used to characterize and record the spectral response of the sensor. It is a PC-controlled single-port USB-interfaced VNA with a frequency range from 40 MHz to 4 GHz as well as the accuracy of +/- 0.5 dB. The VNA is controlled on a PC software named as ShockLine. Configurations such as frequency range and sampling points are set from that software, and measurements are also saved on the user interface. In this experiment, the frequency range is set from 500 to 3000 MHz with 2000 sampling points. All measurement results are saved as CSV format files. The VNA and the sensor are connected with a rigid coaxial cable, and they are fixed onto a customized wood stand. A sample reservoir is placed onto a Lab Jack. The stage of the LabJack can move upward and downward by turning its screw for loading and unloading the sensor. The whole testing system is displayed in figure 4.3. A python script is also developed to automatically extract peak frequency and S11 within a defined range for saving data processing time. The sample of the python code for select the peak point is attached in Appendix A.

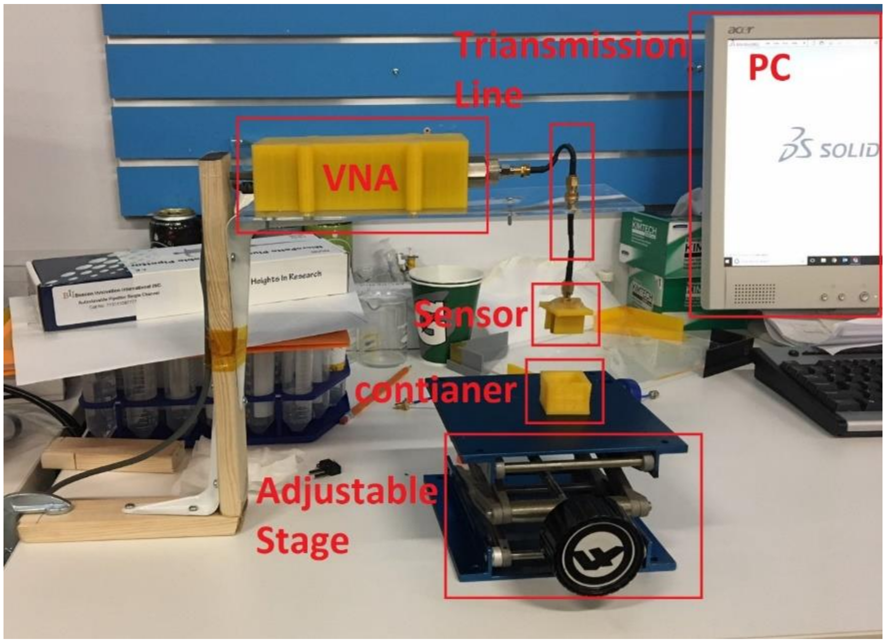

Figure 4-3 : System setup for dip-mode sensor tests

4.1.3.1 Testing Methods

Ethanol solutions, Salt solutions, and different kinds of milk are tested to study the response of the dip-mode sensor on different liquids. The reservoir is first filled with the liquid sample, and it is then placed onto the LabJack stage. The stage is then moved up to let the sensor inserted into the reservoir and immersed into liquid. Four measurements are made and saved to CSV files every 30 seconds. Sensor and reservoir are cleaned by rinsing with DI water after each test.

4.1.3.2 Testing Results and Discussions

A series of diluted ethanol solutions of gradient concentrations are tested by the dip-mode sensor. The concentrations are from 5% to 100% of volume percentage. The results of all solutions are plotted all together in figure 4.4.

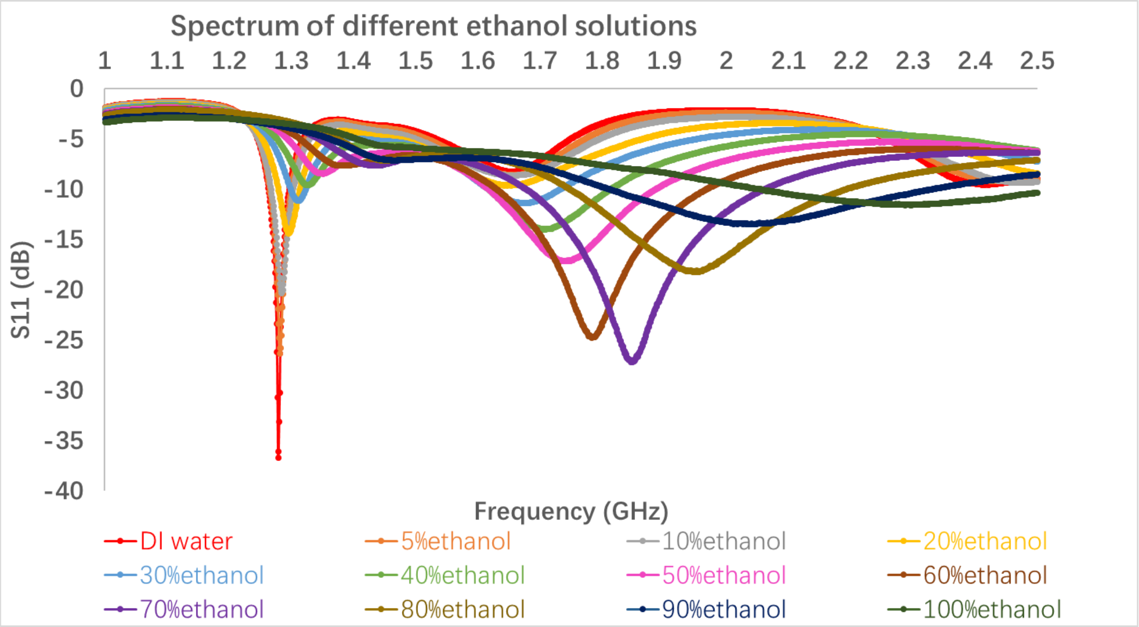

Figure 4-4 Spectrum plot of ethanol solutions

Two evident peaks can be observed from the spectrum. One peak locates at a lower frequency range from 1.2 to 1.5 GHz, and another one is at higher frequency area from 1.5 to 2 GHz. As the ethanol concentration increases, the two peaks have different responses. The left peak will move towards the upright, whereas the right peak moves to the bottom right first and then proceed to upright as the concentration grows.

The frequency trends of both peaks are illustrated in figure 4.5. As the ethanol concentration increases, both peak frequencies will increase nonlinearly. S11 responses of the two peaks are shown in figure 4.6. The S11 value on the right peak of 80%, 90%, and 100% ethanol concentrations are not plotted because S11 values are not extractable for shallow peaks. The S11 value of the left peak increases with higher ethanol concentrations. But the S11 response of the right peak is different. Its value decreases from 0 to 70% of ethanol concentrations and increases above 70 %.

The peak movement might be caused by the permittivity coefficient difference between water (Ɛ=80) and ethanol (Ɛ=24.5). The trend could be explained by the equation 3.5 and equation 3.1 from the last chapter. As the overall permittivity coefficient of the mixture decrease (more ethanol contents with lower Ɛ values), the capacitances of the gap will also decline. That will result in an increase of the resonant frequency of the resonator.

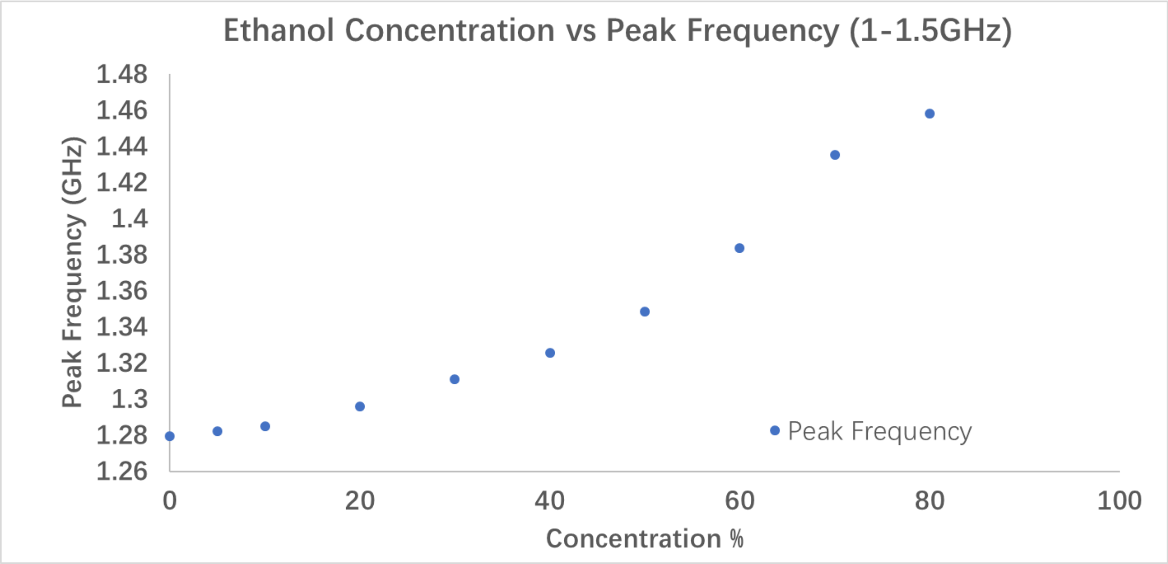

(a)

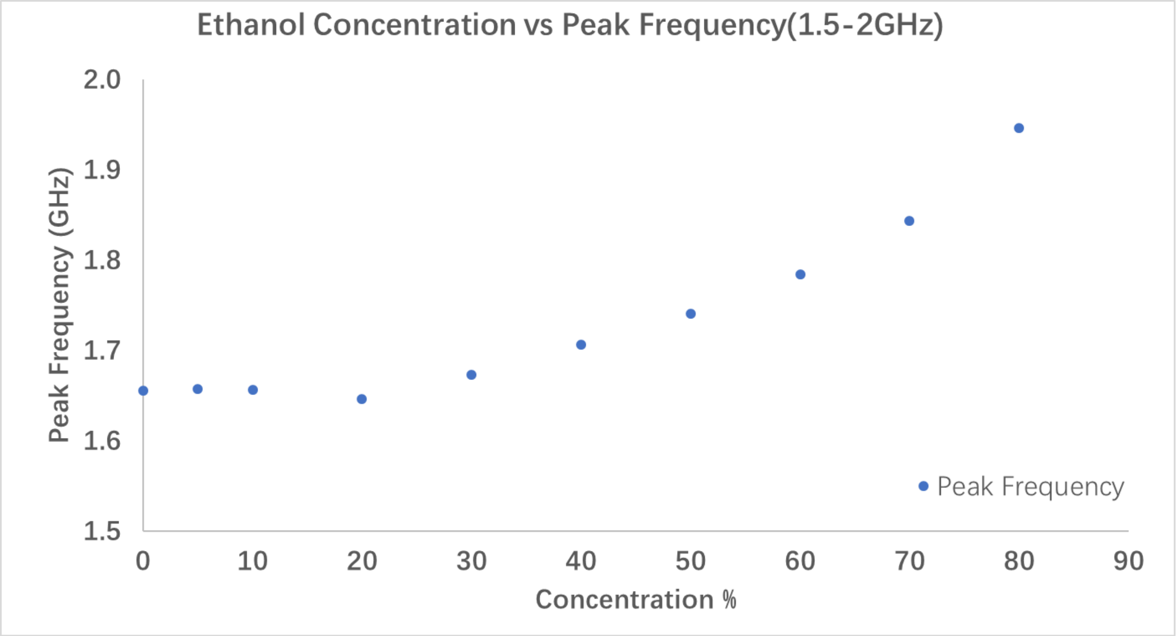

(b)

Figure 4-5 Frequency vs. ethanol concentrations of the right peak. (a)left peak, (b)right peak.

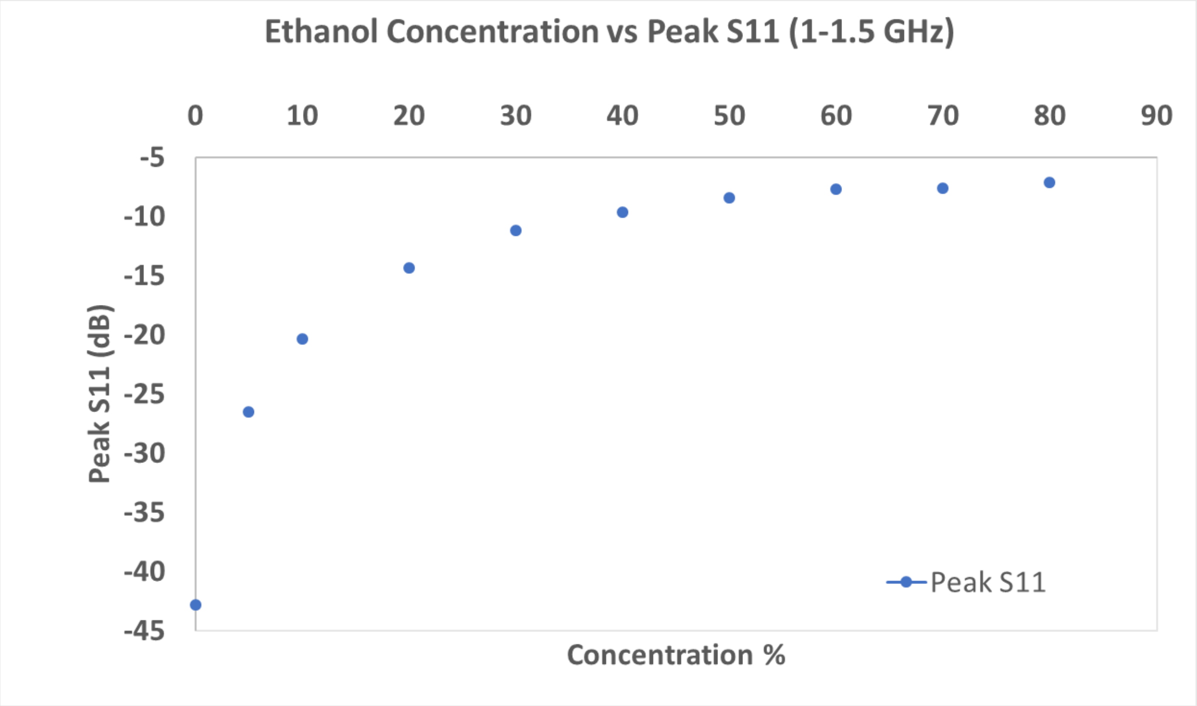

(a)

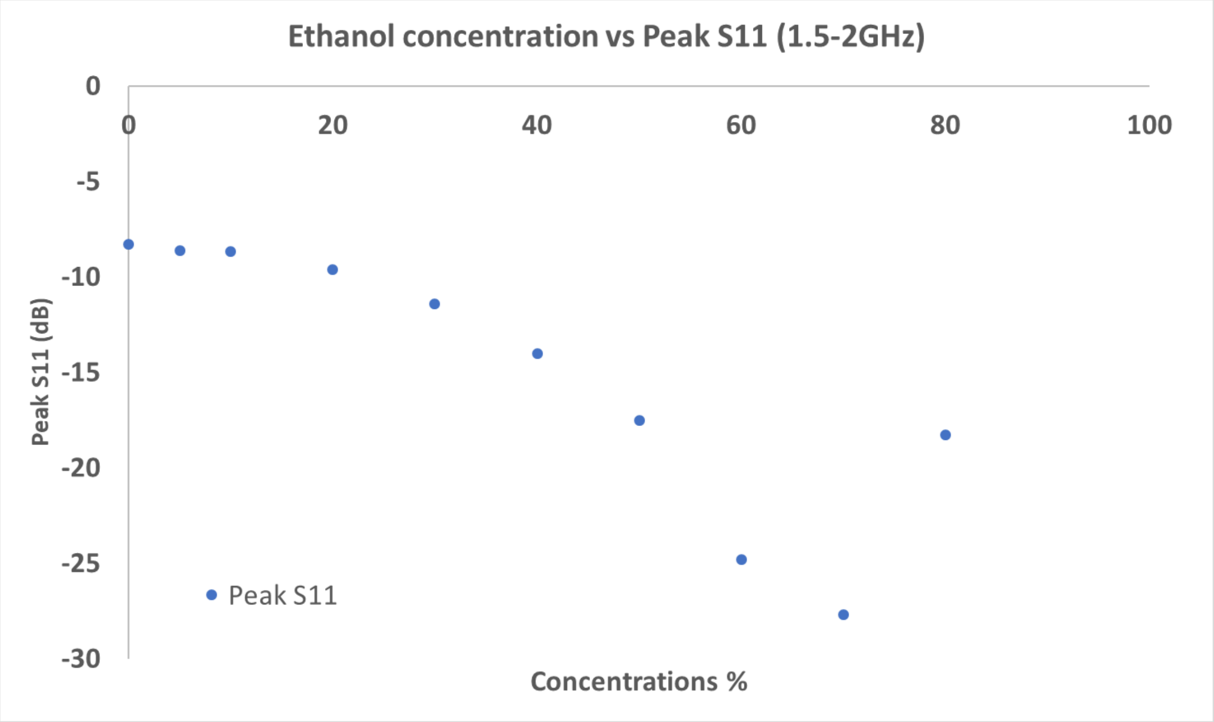

(b)

Figure 4-6 S11 vs. ethanol concentrations of the right peak. (a) left peak, (b)right peak.

Sodium chloride solutions of different concentrations are also tested the dip-mode sensor. The spectrum results are shown in figure 4.7. Two groups of peaks can still be observed. Movements of the peak in x-axis are narrower than the responses of the ethanol solutions. The right peaks are deeper than the ethanol peaks. Some left peaks are not distinct and their frequencies and S11 values are not extractable.

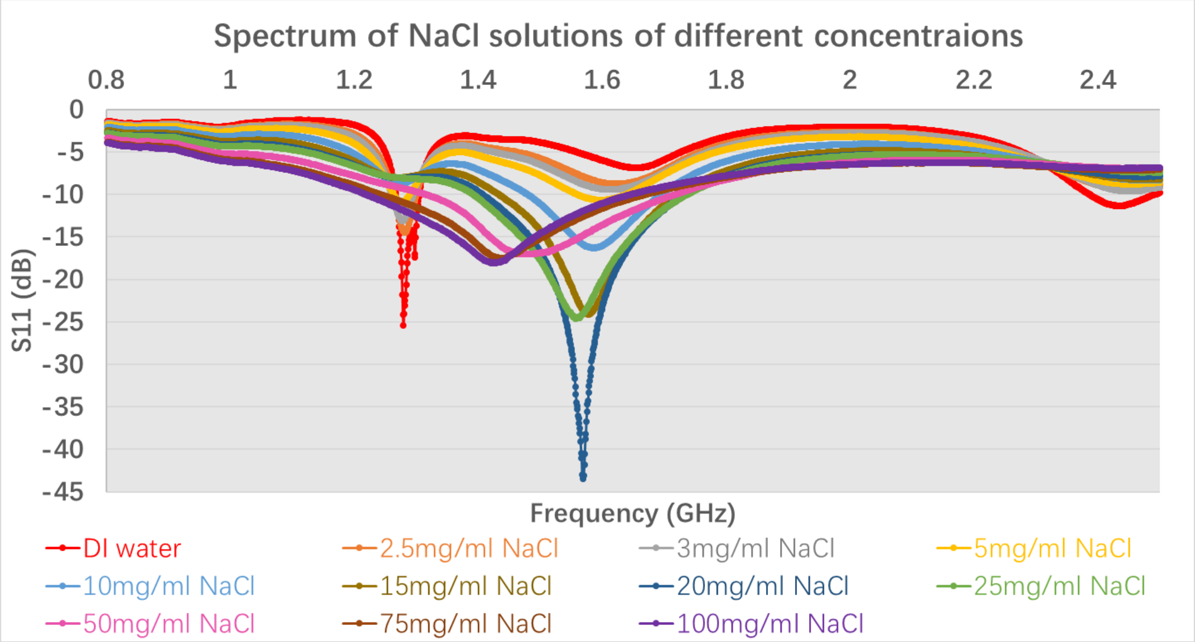

Figure 4-7 Spectrum plot of sodium chloride solutions

Peak frequency and S11 values of NaCl solutions are plotted as figure 4.8 and figure 4.9. The frequency at peak decreases slightly as concentrations increases. The left peak S11 value increases when the concentration increases from 0 to 10 mg/ml. Its trend for higher concentrations cannot be acquired because the peak becomes shallower and finally disappear from the spectrum as the NaCl concentration increases. The trend of the left peak S11 could be predicted from the spectrum as it increases with higher concentrations. The S11 value of the right peak has a similar response with ethanol ones, as they both decrease at the lower concentrations and the S11 value raise at higher concentrations. For NaCl solutions, the valley point is at 20 mg/ml.

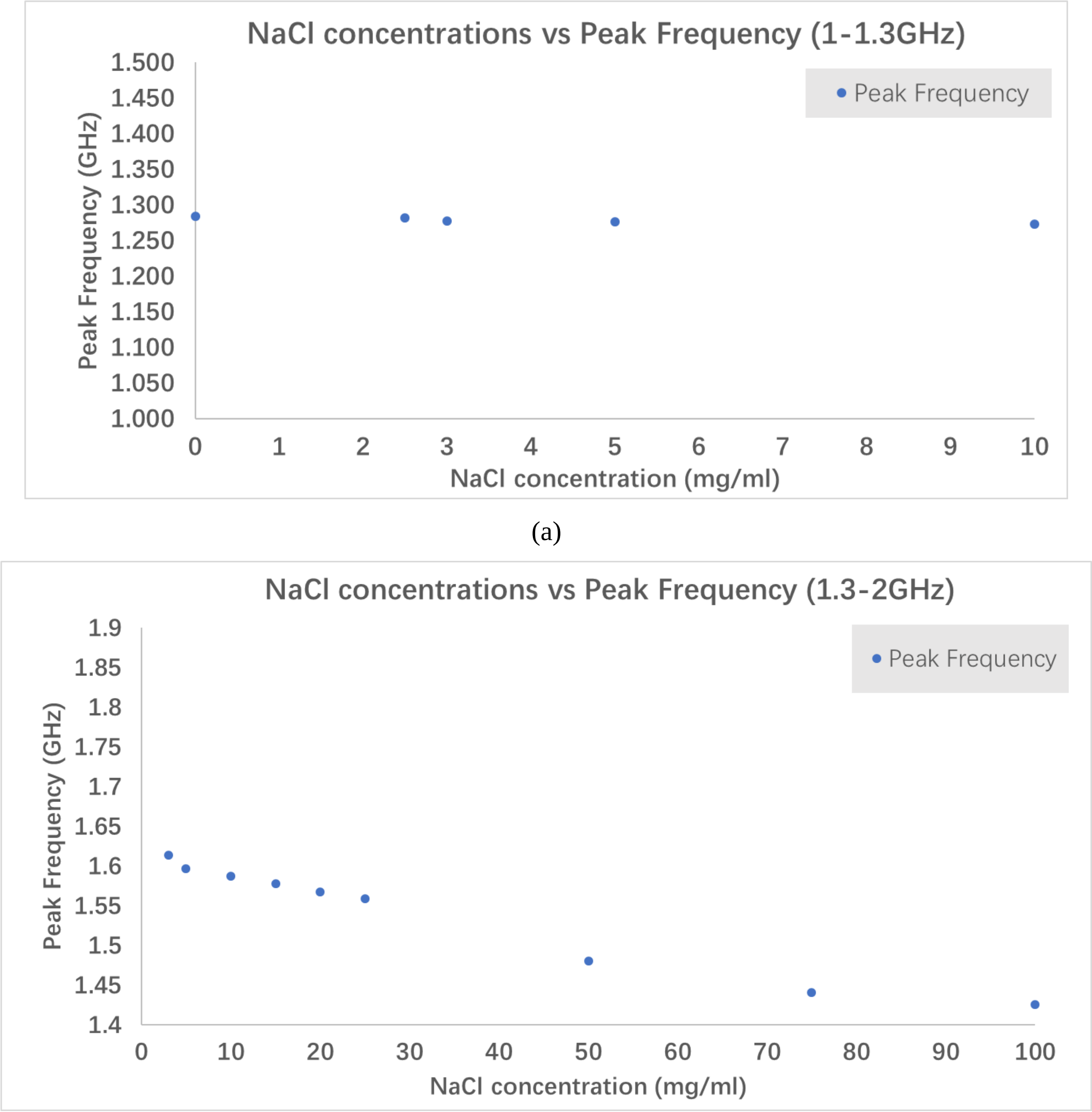

(a)

(b)

Figure 4-8 Frequency vs. NaCl concentrations of the right peak. (a) left peak, (b)right peak.

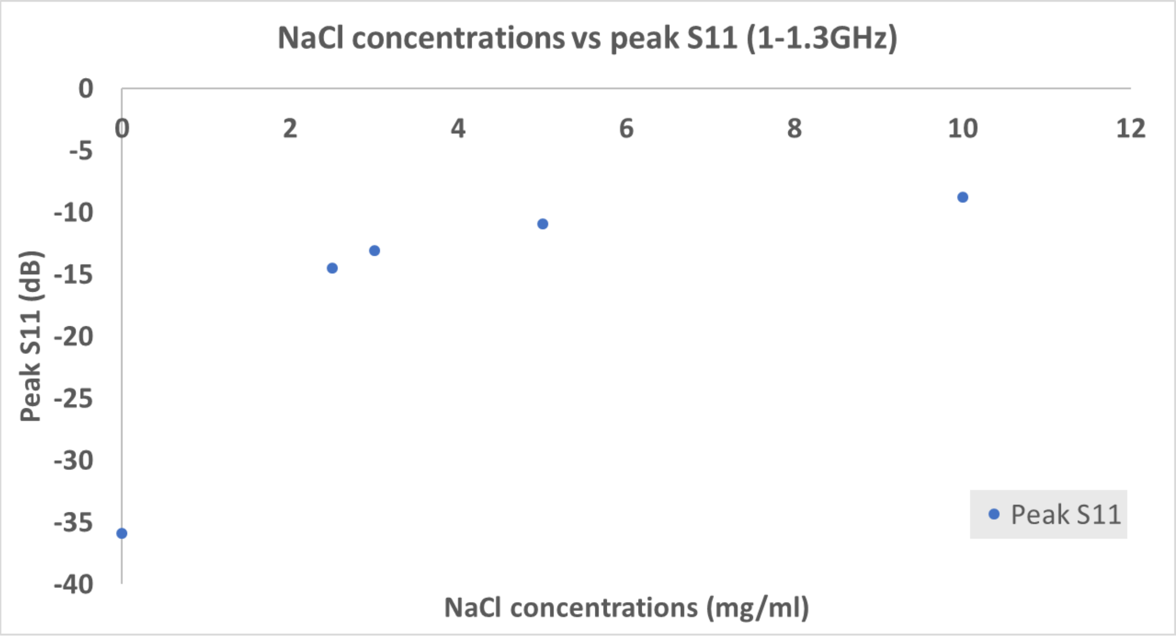

(a)

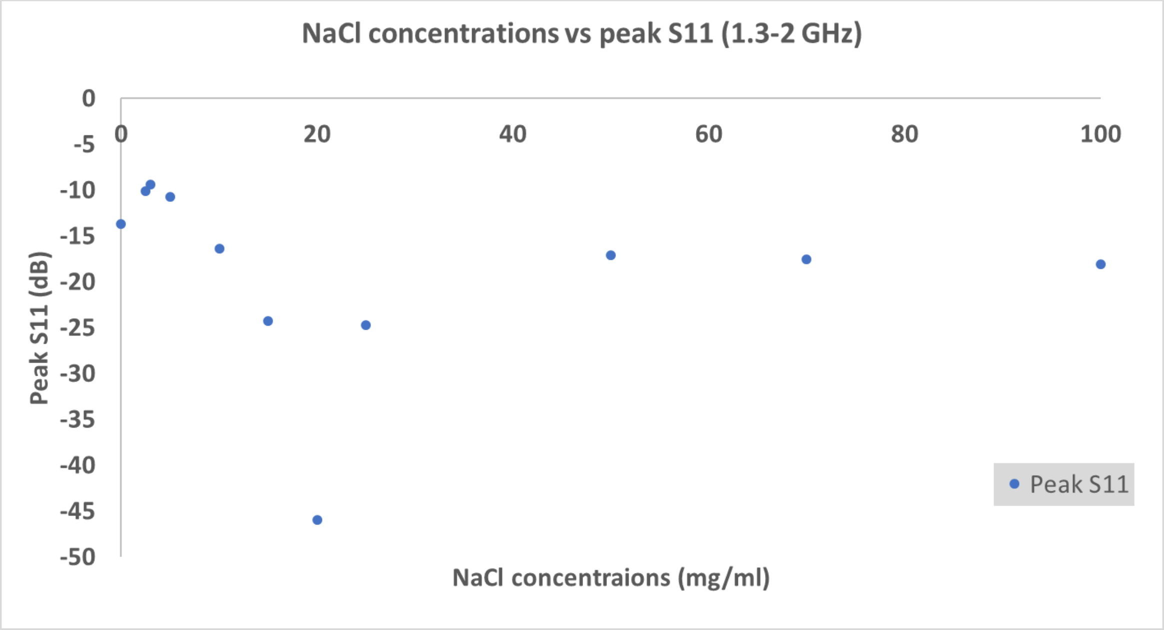

(b)

Figure 4-9 Peak S11 vs. NaCl concentrations of the right peak. (a)left peak, (b)right peak.

Different kinds of natural milks are tested for evaluating the dip-mode sensor's ability to differentiate similar solutions. The spectrum results are plotted as figure 10. Visible differences of peak position could be observed from the spectrum. The frequencies and S11 values of the two peaks for each sample are listed in table 4.1. It can be concluded that this dip-mode sensor can distinguish different milk samples.

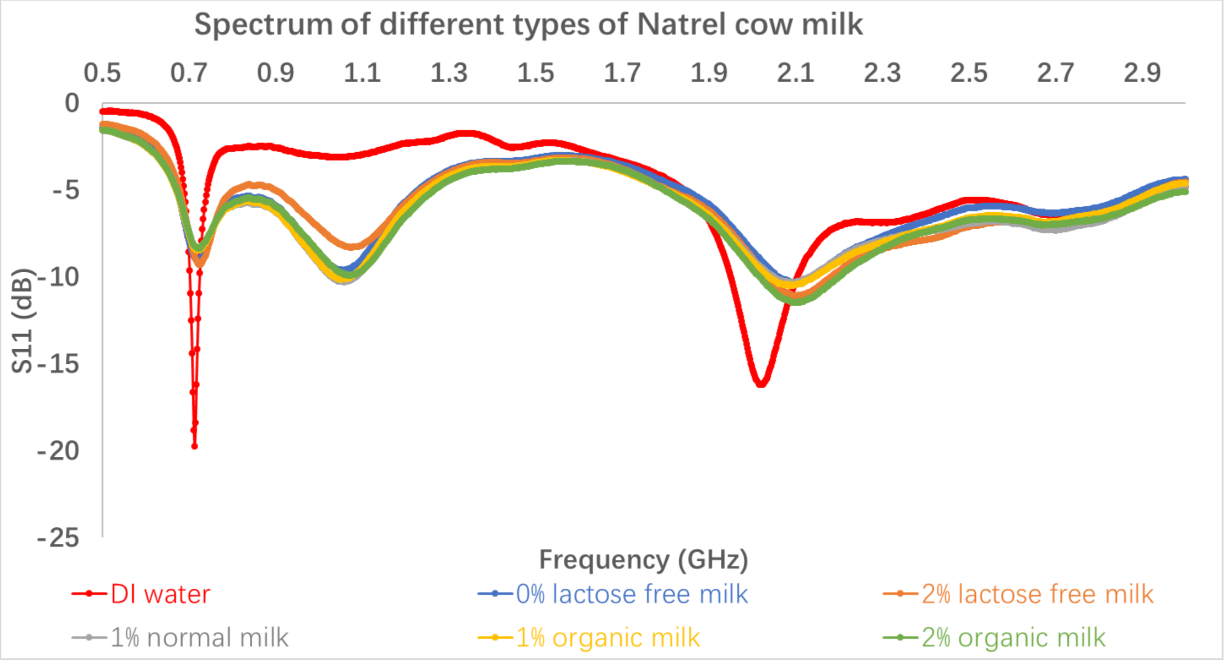

Figure 4-10 Spectrum plot of different kind of natural milks

Table 4-1 Frequency and S11 values of right and left peaks for each milk sample.

	Left peak Frequency (GHz)	Left peak S11 (dB)	Right peak Frequency (GHz)	Right peak S11 (dB)
0% Lactose-free milk	0.72146073	-9.030435333	1.055257629	-9.618042167
1%Normal milk	0.724102051	-8.356624167	1.05657829	-10.290655
1%Organic milk	0.722451225	-8.482469167	1.052286144	-10.14594833
2% Lactose-free milk	0.725422711	-9.302310667	1.07869935	-8.302905333
2%Organic milk	0.723045523	-8.3505494	1.071303652	-9.9093766
DI	0.713206603	-19.78513	1.039409705	-3.126417667

The response of the dip-mode sensor could not simply be analyzed by the RLC theory because both rings are involved, and they both determine the spectral responses. But it can be concluded that the sensor can differentiate liquid sample with different contents, which proves that the sensor could have a potential application on qualitative characterizations such as early warning in food safety industries.

The results from the tests of ethanol and NaCl solution also reveal that the dielectric properties might have a more significant contribution to the frequency shift of the peak, whereas the electrical conductivity might have a higher impact on S11 values. In milk measurements, the peak result of DI is different from the others in ethanol and NaCl test. That is because a different sensor was used to perform tests on kinds of milk. The variance is caused by the fabrication inconsistencies.

4.1.4 Uncertainty and Error Analysis

There are a variety of factors that could affect the testing results of the dip mode sensor, which might cause the signal unstable and reduce reproducibility of results. It is necessary to investigate the source of the uncertainties and errors because the sensor works as an antenna and collects signals as well as the background noises at the same time. Several main factors that contribute uncertainty and errors to the results are discussed as following paragraphs.

Sensor quality inconsistency is one of the main reasons for gaining different testing results from 2 sensors on the same liquid sample. The sensor's quality is determined by the PCB copper trace as well as the soldering joints that connect the SMA connector pin and copper pad. At relative high frequency, the sensor's response is so sensitive that even tiny difference or imperfections during the fabrication process could lead to a significant variance on final results. Those variances may not alter the circuit performance at DC to intermediate frequencies up to several hundred megahertz. However, their effects become unneglectable when the operational frequencies reach up to gigahertz level. Even the tiny variance of inductance or capacitance which are caused by small variations of the shape will lead to a noticeable shift in peak frequency and magnitude. Some main differences of various sensors might come from the different width of the copper trace, different size of the gap, inhomogeneous thickness of the passivation layer and imperfections on soldering works. Though all sensors are made by following the same design and procedures, they might still be slightly different due to the limitation of the accuracy of fabrication techniques. The PCB sensors were initially produced by a mechanical milling machine, by which the copper traces were engraved out from a copper clad board. Noticeable differences regarding the testing results were observed on two sensors that were made by the identical procedures. That might be caused by the variance of the copper trace due to the vibrations during the milling process. The consistence of multiple sensors' results was improved significantly by using industrial foundry. However, signal variances between different can still be observed, which might be caused by the soldering quality variances among sensors. The SMA connector and copper trace are connected with tin shouldering joints, and it is electrically short at DC.

However, at RF range, the joint is no longer short. Small impedances will exist at the joint which will affect the results.

Temperature is another main factor that may affect the measurement results. That is caused by the change of the dielectric property of the substance as the function of temperature. The response of the peak frequency in the spectrum has been discussed in chapter 3, as the resonant of the loop-gap ring is determined by the dielectric coefficients of the substances that exist beside the gap and copper trace. As a result, the peak position in a S11 vs. frequency plot of the same liquid sample might shift with different temperature. Previous research has proven that both frequency and S11 of a SRR sensor would change nonlinearly as the temperature increases (Wong et al., 2016). In this experiment, the tests were performed in the lab of constant temperature at around 25 ^{o}C.

The liquid surface level can change the peak position during or between each test. That could also be explained by the working principles of the sensor. As discussed in Chapter 3, the capacitance and inductance of the gap loop ring are determined by the dielectric properties of the surrounding substances, which will eventually control the shape of the spectral response as well as the peak frequency. In this case, the sensor was dipped directly into the liquid, the portion of the sensor that is immersed into the liquid might vary. That could lead to the differences between capacitance and inductance even between 2 same liquid samples. Therefore, though the sensor is dipped into the same liquid sample twice, the spectrum results might be different due to the liquid surface level effects. In this experiment, the sample reservoir was filled before each dipping to assure that the liquid surface is identical. But variances of spectrum among repeat tests of the same liquid sample were still observed, which might be probably caused by the liquid surface effects.

The imperfection of the coaxial cable is another main factor that might affect the spectral response because the impedance of transmission line could change while cable being moved. A long and semi-rigid coaxial cable is applied between the sensor and VNA at the beginning of the research, and the sensor was dipped down into the liquid instead of moving up the reservoir. Apparent peak movement on the spectrum can be observed when the cable is bent. That issue is solved by replacing the cable with a rigid cable and changing to the dipping method. That phenomenon can be explained by the transmission line theory that was discussed in chapter2. In an ideal condition, the capacitance and inductance along a transmission line would not change. However, in real condition, the transmission line's capacitance will change when it is bent because the distance between the central copper core and woven copper shield changes as well. The impedance change could influence the spectrum response, which might be the reason for the peak shift.

Broken and pollution of the passivation layer could shift the peak location as well. Though the passivation layer is made of the epoxy polymer which has high chemical durability, visible degradation of the passivation is observed after a period of tests, as copper trace surface exposed on some areas of the surface. That might be because of the dissolution of the layer into the organic solvents such as ethanol or methanol. The sensor could also be polluted by some sticky substances because they would adhere to the sensor's surface. It usually happens while testing on milk or honey samples. That makes it hard to remove those remaings by normal cleaning procedure. Those remaining materials might cause the signal drift over tests due to accumulation or release processes. Therefore, the sensor was carefully cleaned before each test to decrease the pollution effects. Only single sensor is applied to perform tests on the gradient-concentration test for each material, to avoid the variance issues between different sensors. But the degradation effect cannot be avoided in this case.

External RF interference could also influence the spectrum of the test. In this experiment, the sensor works within a broad frequency range from 500 – 3000 MHz. There are many electronic devices that communicate through RF bands or emitting RF waves within that range, such as cell phones, personal computers, microwave oven and any electronic devices that have built-in Bluetooth or Wi-Fi. The experiment set up is placed as far as possible from those electronic devices, however, background noises still exist because RF waves can penetrate relative long distances. Isolation of the wave by adding a metal case is not feasible because if any metal exists beside the sensor, it will couple the wave from the excitation ring and significantly change the spectrum response. Therefore, during this experiment, the only approach to reduce the external RF effects was to keep away the electronic devices away from the test set up.

4.2 Channel-mode Sensor

A microfluidic channel-based microwave sensing system is implemented in this chapter. Microfluidics sensing system is attracting increasing interest in both research and industry fields. It has unique advantages over the dip-mode system regarding the size, performance and the volume of sample required. Two types of materials, Polydimethylsiloxane (PDMS) and acrylic tape, are used to make microfluidics channels. The channels are then bonded to the PCB sensor made from Chpater2. Their performances are evaluated and compared by experimental tests on real liquid samples, such as deionized (DI) water, salt solutions, and ethanol solutions. Testing results reveal that the tape-based channel system is sensitive enough to differentiate the solutions under test, but for PDMS channels in comparison, it is not capable of discriminating the sample due to the significant variation between the channel's and sensor's size.

4.2.1 Overview of the Channel-mode Sensor

The channel-based sensor has a similar structure and the same working principles as the glass-based ones. The channel is aligned exactly above the gap area. Liquids that flow within the fringing filed generated by the gap-ring-resonator, could change the capacitance of the resonator. Therefore, the peak frequency and S11 parameter at the peak will shift as well. Figure 4.11 illustrates the fringing field that exits above the sensor gap region.

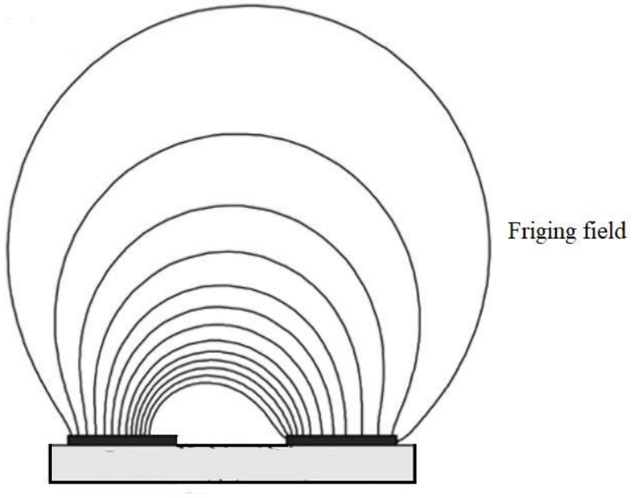

Figure 4-11 Schematic interpretation of the fringing field exiting above the cap region (Li, Larson, Zyuzin, & Mamishev, 2006).

Channel-based sensors have many advantages comparing with the dip-mode sensors. First, it requires fewer volumes of samples compared with the dip mode. The sizes (length by the thickness of the channel's cross-section) of the channel used in this experiment range from 200 um*50 um (for PDMS channels) to 1 mm*0.1 mm (for tape-based channels). Channel-based sensor usually requires 1-5 ml of liquid to perform a test, whereas a dip-mode test needs around 50 ml. The tape-based sensors have absolute more benefits when the volume of sample is limited. Second, the noises decrease dramatically in the tape-mode sensor. Only one peak is observed within the frequency range during the experiment, and it is more stable compared with the dip-mode. That is because that, in tape-mode, there is only one variable which is the capacitance of the resonator, instead of multiple shifts of capacitances and inductances within the inner ring and between the two rings in the dipping mode. Third, channel-based sensors are more user-friendly regarding the testing and cleaning. Testing with channel-based sensors is semi-automatic. The liquid sample is pumped into the channel, and DI water is primed to wash the sensor. That makes it a more realistic option for a developing a testing a product. Finally, studying the channel-based sensor can help understand the working mechanism of the ring resonator, which is one of the objects of this research.

4.2.2 PDMS Channel-based Sensor

A PDMS-channel-based sensing system is developed first. It consists of the PCB sensor and PDMS microfluidic channel. Direct PDMS-epoxy bounding and PDMS-PDMS bounding are evaluated in this experiment.

A PDMS-based microfluidics chip with a single channel is made using the standard soft lithography method. A silicon-based master covered with SU8 photoresist was made first. Uncured PDMS mixture was poured onto the master, and they were then cured on a hot plate at 190 ^oC for 5hrs. The cured PDMS channel could be peeled off from the wafer after cured.

The PDMS channel is bounded onto the epoxy surface first, but a PDMS-PDMS bound is then applied due to its stronger bonding strength. PDMS microfluidic channel is bounded to a clean epoxy surface using oxygen plasma at 500 mTorr for 2 minutes. However, leakage is observed around the channel while injecting liquid sample at the flow rate of 10 μL/min. Though PDMS will become adhesive after the plasma treatment, the bonding between the PDMS and epoxy passivation surface is too weak for enough sealing strength. That might be caused by the surface property difference of the two materials. Therefore, the PDMS-PDMS bound is used to stick the channel onto the PCB sensor. Instead of the direct bonding, a thin PDMS layer is spin coated onto the top of the sensor surface using a spin-coater at 4000 rpm for 3 minutes. The layer is cured at 190 ^oC for 5 hours. Two PDMS surfaces are bounded using oxygen plasma at 500 mTorr for 2 minutes. The PDMS-PDMS bounding has a significantly stronger bonding strength than the PDMS-epoxy bound, no leakage is observed during the test. The final assembly is illustrated in figure 4.12.

Figure 4-12 Picture of a PDMS-channel sensor.

The performance of the PDMS-channel sensor is not as good as expected. No distinguishable peak shift can be observed for the reference samples such as DI water and ethanol. That might be caused by the considerable size difference between the gap and channel. The channel used in this experiment is 200 μm wide and 50 μm thick, but the gap is 1 mm. The capacitance change is not big enough to be captured by the VNA because of the limitation of its resolutions. However, the size of the PDMS channel cannot reach to 1 mm because it will collapse if the channel is too broad. Therefore, the PDMS channel is not practical for the PCB sensor, other material and fabrication techniques need to be explored.

4.2.3 Tape Channel-based Sensor

A tape version of the microfluidic channel is developed to overcome the low sensitivity issue. The sensor is still in channel mode, but it uses a double-sided tape for forming the boundary and seal the channel. The cross-section of the sensor has a sandwich structure, which consists of an acrylic cap on the top, a channel cut from double-sided tapes and the PCB sensor on the bottom. The channel is aligned exactly above the gap which lets the liquid flow through the fringing field. The cross-section view and 3D schematic structures of the sensor are shown in figure 4.13.

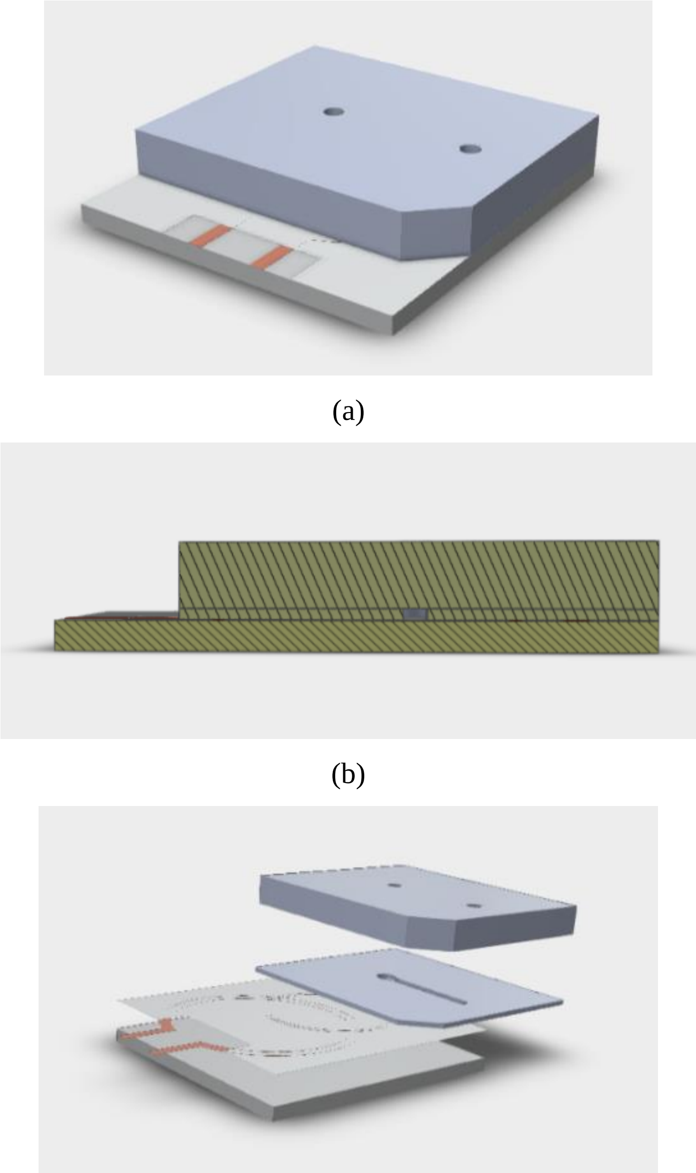

(a)

(b)

(c)

Figure 4-13 3D assembly and structures of the channel sensor composed by using SolidWorks. (a) view of the assembly of the channel sensor, (b) cross-section view of the sensor, which a sandwich structure with acrylic cap on the top, tape in the middle and PCB sensor at the bottom, channel is in the intermediate layer, (c) explode view of the layer structures of channel sensor, from the top to the end are acrylic cap with inlet and outlet holes, tape with channel, passivation layer, SRR copper trace and FR-4 substrate.

Medical grade (ARcare 90106) polyester double-sided adhesive tapes were adopted as the channel substrate. The thickness of singe tape is around 0.025 mm with a transparent polyester film in the middle and two acrylic hybrid adhesive layers on both sides. However, it is too thin for sealing the channel because the PCB board is not perfectly flat, with the copper trace around 0.0356 mm higher than the base. Leakage may happen if only one layer of the tape is used. In this experiment, four layers of tape are stuck together forming a 0.1 mm thick layer. A 1 mm wide channel is laser cut on that layer. The sheet is then attached to the PCB sensor with the channel aligned exactly above the gap. Finally, a 3 mm thick acrylic board with two laser cut holes with an inlet and an outlet hole respectively, is placed on the top of the tape. The adhesive material is pressure sensitive, so the acrylic top and PCB board needs to be pressed by using a c-shape clamp for better sealing. The finished sensor assembly is shown in figure 4.14.

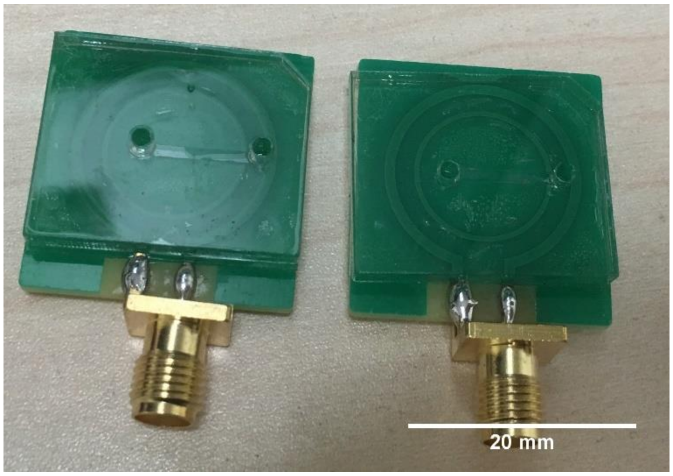

Figure 4-14 Two identical finished tape sensors, the channel can be seen clearly on the left one.

4.2.4 Testing with the Tape-channel-mode Sensor

A testing system using the tape-channel sensor is developed. The system consists of a pump, a sensor, tubes, and a VNA with driving PC. Figure 4.15 shows the sensor and system schematic structure. The liquid sample is pumped from sample reservoir and injected into the sensor through plastic tubes by VWR variable-speed peristaltic pump. Wastes are collected into a waste reservoir. The sensor is connected to the VNA directly with type N to SMA sensor to keep the transmission line as short as possible. Frequency range is changed to 1.4 to 3 GHz because the channel-mode sensor has only one peak that locates within that region. Other configurations of the VNA, measurements and result saving process on PC software are the same as the dip mode. System setup for a tape-channel sensor is shown in figure 4.16.

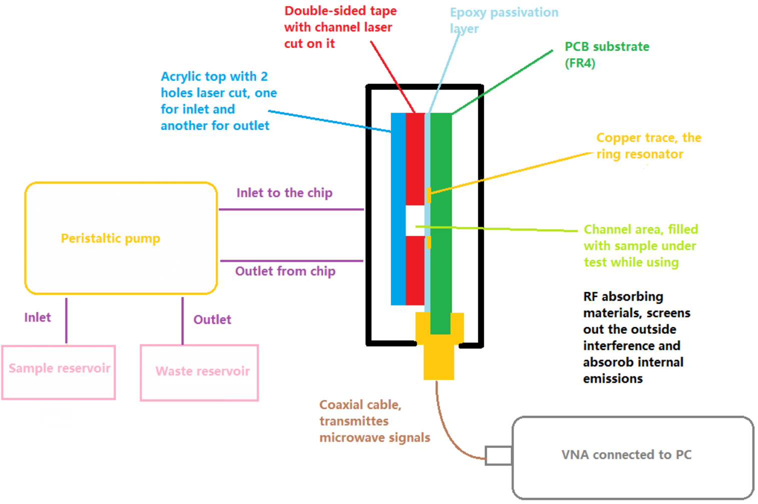

Figure 4-15 Sensor cross-section view and testing system structure.

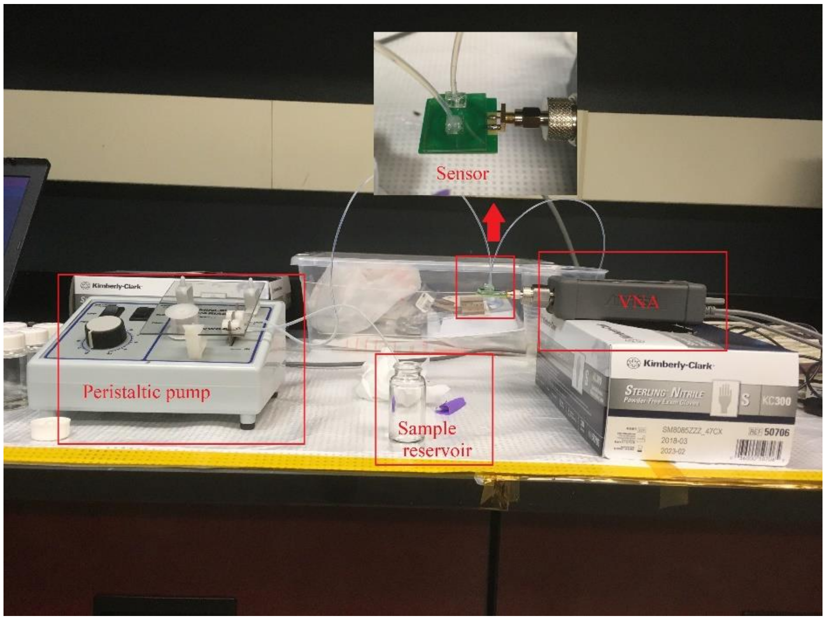

Figure 4-16 Picture of the experimental setup for the channel-mode sensor.

4.2.4.1 Testing methods

The sensor's performance is evaluated by testing several reference solutions such as DI water, pure ethanol, and salt solutions. The liquid sample is first pumped into the sensor's channel at the lowest flow rate. Then four repeat measurements are made and saved every 30 seconds for each sample. Air is primed into the channel for 30 seconds after finishing each sample, to push out the remaining. The tube and channel are also washed with DI water for 30 seconds before testing any new sample. Peak frequency and S11 are extracted from the CSV result using the same python script used in dip mode. Same procedures are performed on ethanol and salt solutions of gradient concentrations, for investigating the qualitative effects of dielectric coefficients and electrical conductivities on spectrum response.

4.2.4.2 Testing Results and Discussions

Ethanol solutions of gradient volume percent from 10% to 100% were tested by the channel-based sensor. Two groups of peaks can be observed from the spectrum plot figure 17. The two group of peaks have a different response of the samples. The left peak gradually moves towards upright as the concentration increases, whereas the right peak barely moves. So only the left peak is used for the response analysis. Both peak frequency and peak S11 increase as the concentrations rise, but S11 has a better linear relation with the volume percentage.

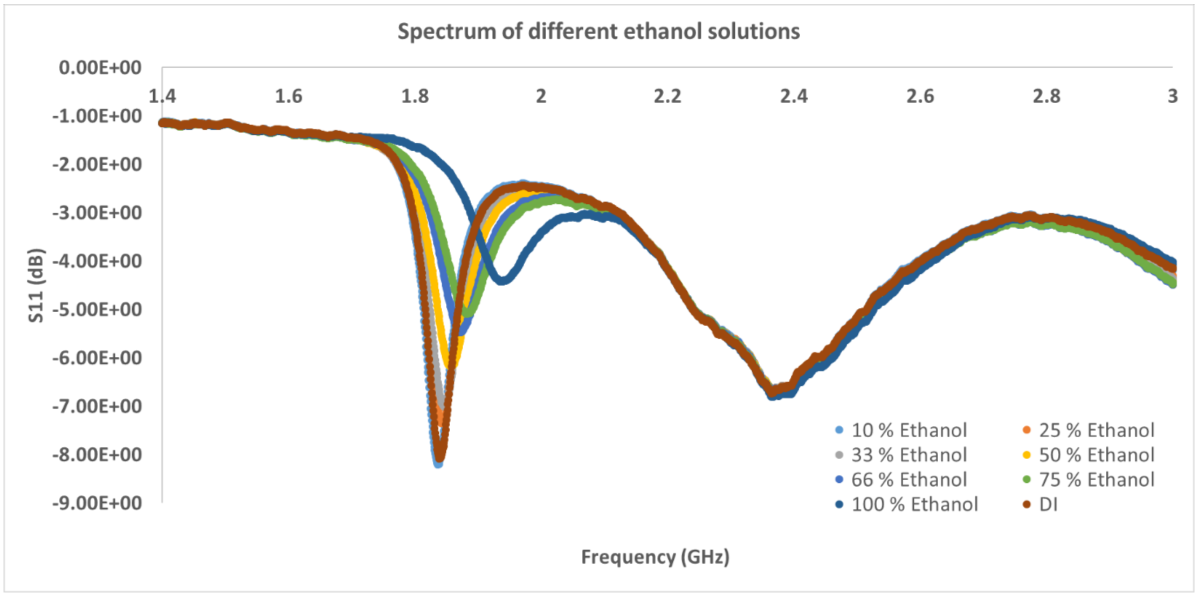

(a)

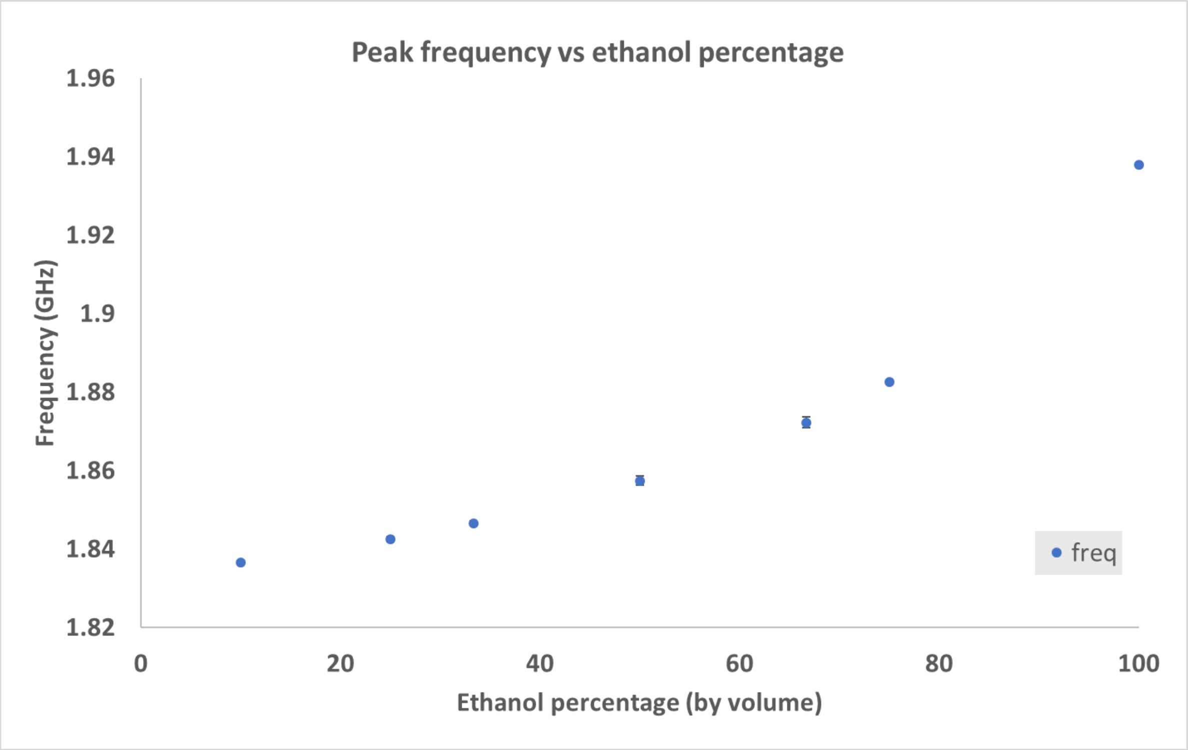
Peak frequency vs ethanol percentage
Frequency (GHz)
1.96
1.94
1.92
1.9
1.88
1.86
1.84
1.82
0
20
40
60
80
100
Ethanol percentage (by volume)
● freq

(b)

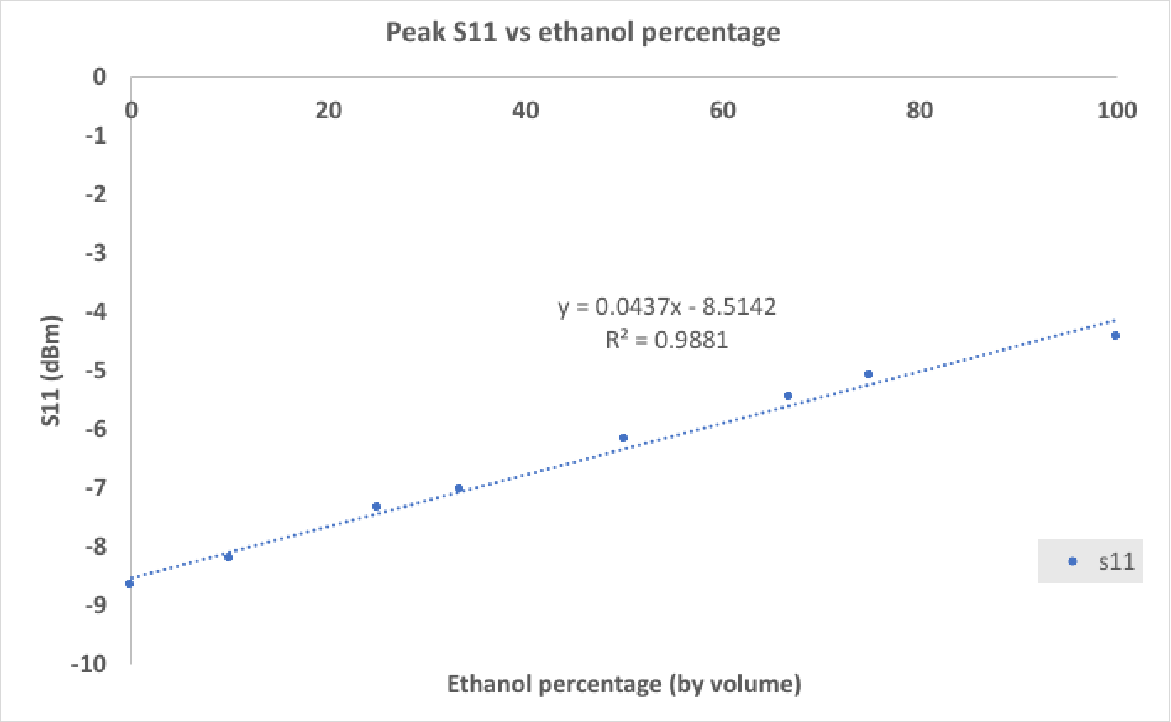
Peak S11 vs ethanol percentage
S11 (dBm)
0
-1
-2
-3
-4
-5
-6
-7
-8
-9
-10
0
20
40
60
80
100
y = 0.0437x - 8.5142
R² = 0.9881
● s11
Ethanol percentage (by volume)

(c)

Figure 4-17 Peak frequency and S11 of ethanol solutions: a- spectrum plot of ethanol solutions, b- the plot of peak frequencies versus ethanol volume percentage, c- the plot of peak S11 values versus ethanol volume percentage.

The spectrum of NaCl solutions has a similar patter as the ones of ethanol solution (figure 18). Two groups of peaks can be observed, and only the left peak moves with different samples. The peak response of the concentration growth is different from the ethanol. Peak frequency does not indicate a clear trend as concentration raise, it first increases at low concentrations and then decreases above 20 mg/ml. The S11 of the peak has a more significant trend as the NaCl concentration rise up, as it moves nonlinearly with the concentration.

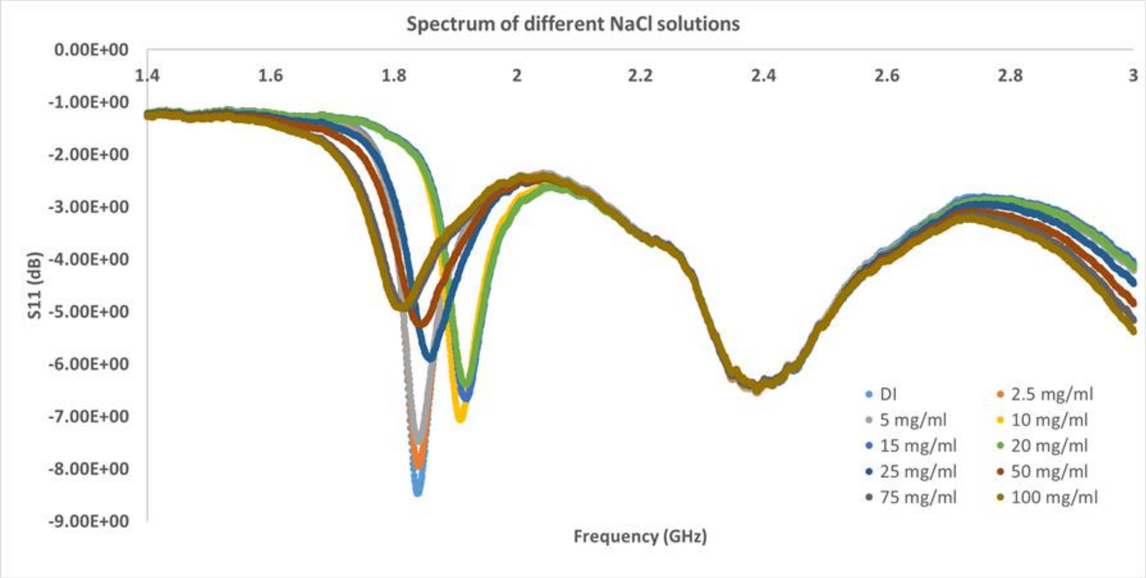

(a)

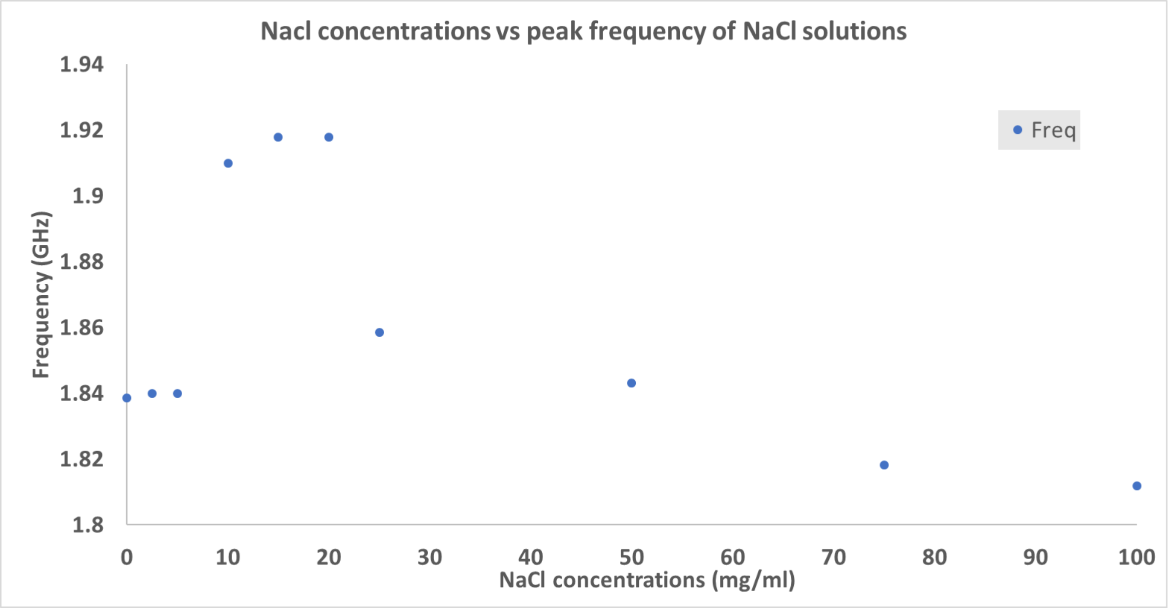

(b)

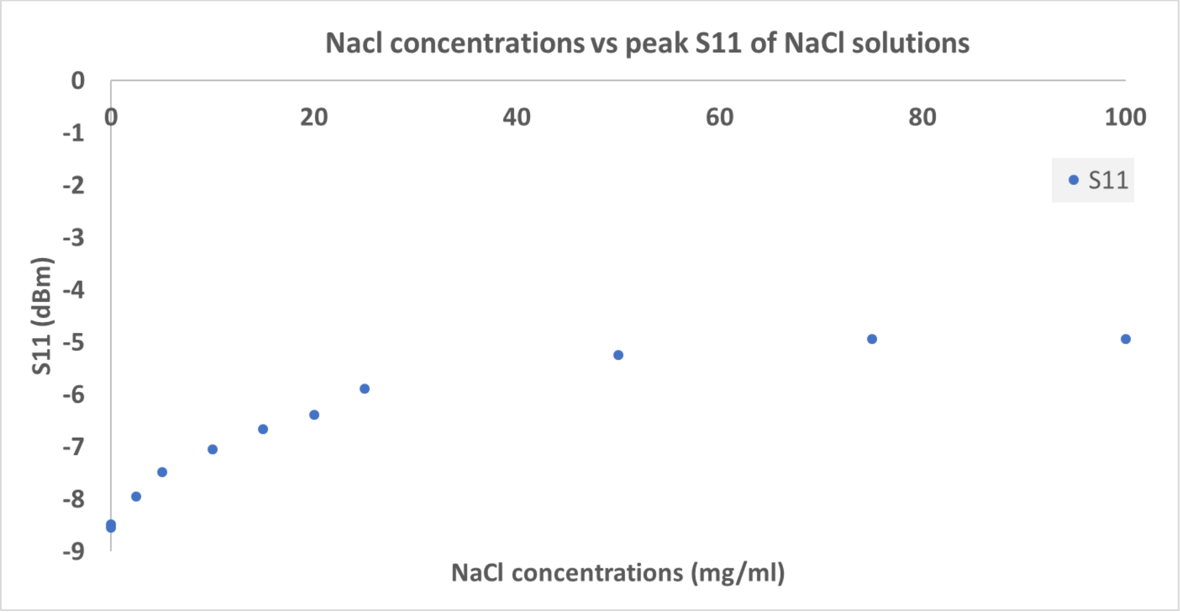

(c)

Figure 4-18 Peak frequency and S11 of NaCl solutions: a- spectrum plot of NaCl solutions, b- the plot of peak frequencies versus NaCl concentrations, c- the plot of peak S11 values versus NaCl concentrations.

Milk dilutions are also tested with the sensor. Results are interpreted as figure 19, with only peak area displayed. The movement of the peak for milk samples is much smaller than the peaks of ethanol and salt solutions. The peak moves to the up right as the milk percentage goes up, which is similar to the ethanol dilutions. Both peak frequency and peak S11 increase linearly as the concentrations, but the S11 has a better linear relationship.

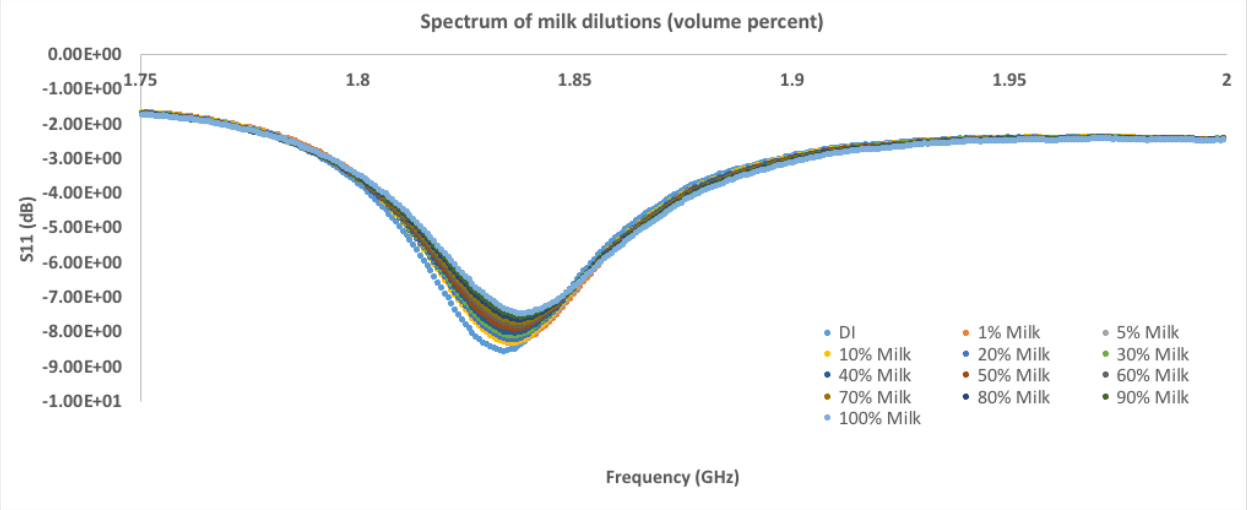

(a)

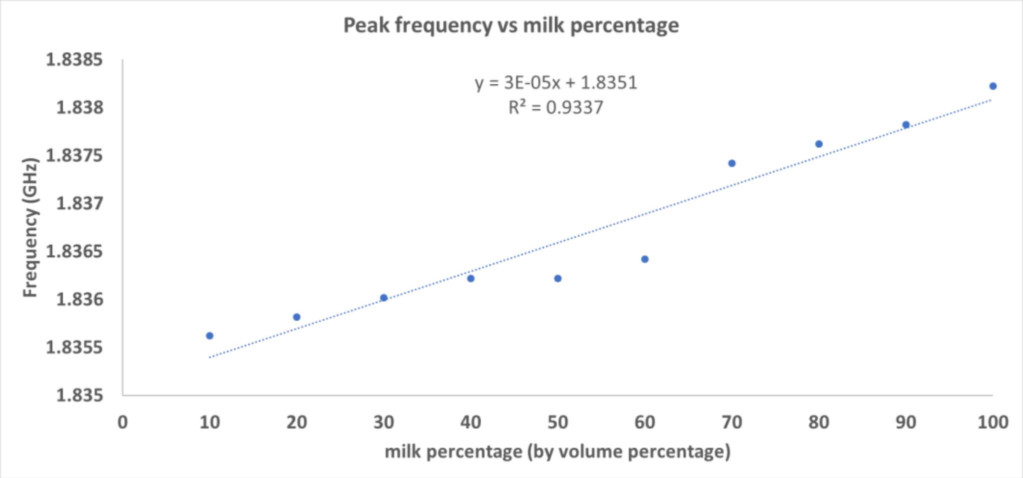

(b)

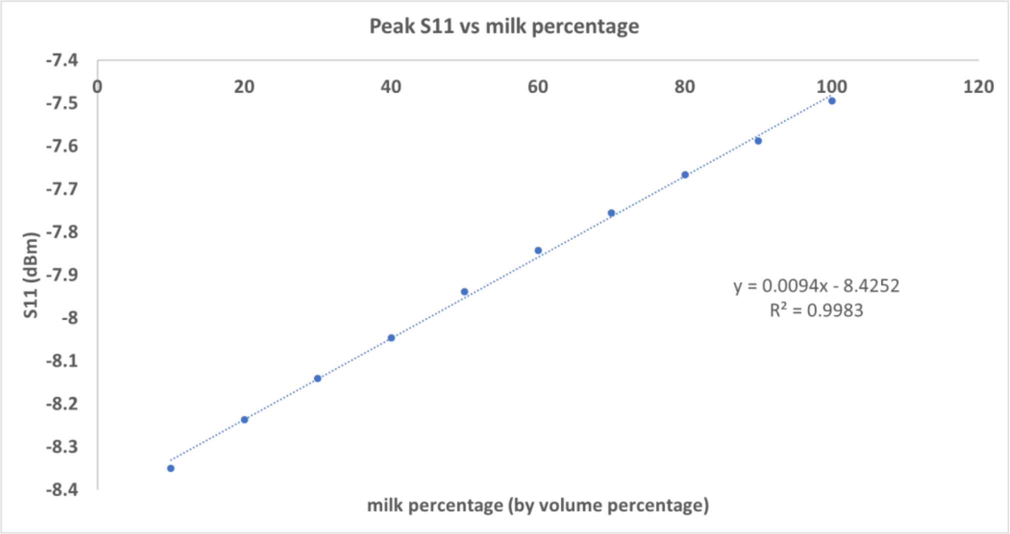

(c)

Figure 4-19 Result of milk dilution tests: a- spectrum plot of diluted milk samples, b- the plot of peak frequencies versus milk volume percentage, c- the plot of peak S11 values versus milk volume percentage

As displayed in the spectrum results from dip-mode sensor tests, the spectrum has an active peak that changes with the dielectric properties of the liquid under test as well as a fixed peak that barely moves through all the experiment.

The active peak at lower frequencies is caused by the impedance change of the inner ring, which was discussed in Chapter 3. The peak frequency trend of concentrating ethanol solutions and the peak S11 shifts over concentrating NaCl solutions can be explained by the RLC theory. As the ethanol content increases, the gap capacitance will drop at the result of the reduction of liquid sample's relative permittivity referring the euation 3.5. Thus, the resonant frequency will increase. For NaCl solutions, as it becomes concentrated, the electrical conductivity increases. That leads to impedance decline at the resonant frequency which is interpreted as R in Figure 3.3.

The fixed peak at the higher frequency might be caused by the formation of additional RLC circuits, which is also observed in the dip-mode sensor. But the peaks in the channel-mode are more stable than the dip-mode versions because the surrounding environments of the dip-mode SRR are consistent through all tests.

4.2.5 Uncertainty and Error Analysis

The tape channel-based sensor has similar effect factors on uncertainty and errors while testing because the same PCB resonators are applied to both modes. The same factors include sensor quality variances, temperature effects, and external RF interferences. However, liquid surface effect and passivation layer decade will no longer influence the tape channel sensor because the testing liquid is constrained within the channel region, and it would never contact with the metal sensor. The coaxial cable effect is not an issue for tape version system either, because the sensor is connected directly to the VNA. However, the tape channel method is still not perfect. Some new factors might contribute errors and uncertainties to the system such as channel misalignment and dielectric effect of ambient environments.

Channel misalignment during the fabrication process is one of the main reasons for the inconsistency between different sensors. Though the misalignment of channel and gap would not affect reproducibility of the measurement results, it will cause the variance between different sensors. That is because that the response of the channel sensor is only determined by the overall dielectric properties of the substances that exist within the wave penetration region above the gap. The channel should ideally be aligned exactly above the gap; however, they are not usually perfectly aligned due to the human error. In reality, the sensor is sensing the combination of the liquid within the channel as well as the channel boundary, as shown in figure 4.20. Acrylics have significant different permittivity constant value with the water's value. As a result, the variance of testing results of the same sample among different sensor may occur due to misalignment of the sensor and channel.

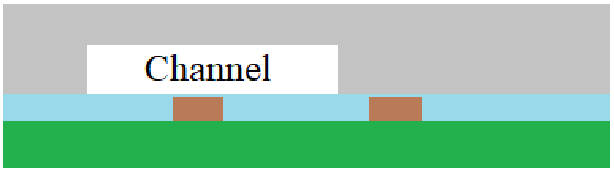

Figure 4-20 Schematic diagram for interpreting the misalignment situation during the fabrication process.

Coupling and dielectric effects of the ambient substances is another main reason that causes the sensor's measurement unstable. During the test, a significant change in spectrum plot can be observed when there is a plate or board placed underneath the PCB sensor. If a metal board is placed under the sensor and it is close enough, there will be no peak on the spectrum. If a nonconductive material, such as a wood board or book, is put under the sensor, the will peak still exist, but it will move significantly compared with original one when nothing existed around the sensor. Those phenomena are caused by the coupling effects of the surround materials. The outer ring that is also known as the excitation ring emits RF wave while working, and all the waves are supposed to be ideally coupled to the inner ring. However, if there is a metal placed beside the outer ring, nearly all the waves would be coupled to the metal instead of the inner ring. That explains why no peak can be observed on the spectrum when a copper board is placed under the sensor. A nonconductive material near the copper trace can change its inductance and capacitance, which is the reason for the peak shift when book or hand was near the sensor. In this experiment, the sensor is kept away from any metallic material, and the sensor was also kept 10 cm away from the working bench.

Chapter 5 Development of a Customized Vector Network Analyzer

A vector network analyzer (VNA) is a typical electronic measurement device for microwave network characterization which can measure the S-parameters of a passive RF component. In this thesis, a commercial VNA is applied for measuring the S11 values of the microwave sensor at various frequencies and interpret them as the spectrum which can discriminate and characterize the liquid samples. A commercial grade VNA is typically designed for generous measurements of RF components. However, when it is used for specific applications, its advantages such as high dynamic range, abundant functionalities might not be required. And sometimes its advantages could be limitations because of high cost, bulky size and complicated structure of a commercial VNA. They also limit their development on making portable and affordable LOC platforms. Therefore, there is a need for developing customized VNAs for specific applications. A customized vector network analyzer circuits are developed in this chapter for the microwave sensing system. The new VNA system has several improvements regarding the frequency range, cost, and accuracy, compared with the circuits produced in the previous work. The performance of the new developed VNA is validated by comparing its results with the commercial VNA.

5.1 Motivations of Developing an Improved VNA Circuit

A microwave reflectometer and DAQ system were developed in previous research (Yesiloz et al., 2015). It uses a VCO as the microwave source that is controlled by a digital to an analog module in a National instrument DAQ system. A bidirectional coupler is applied to extract and separate the forward and backward microwave signal. A gain detector is used to convert the power difference of the microwave signals from the 2 channels of the coupler into DC voltages which is sampled by an analog to a digital module, and the data is sent to PC for post processing. The system is simple and affordable, and it has a rapid response because of its high sampling rate. It can differentiate oil and water, and it is used at a droplet counter combing with a glass-based sensor with droplet generating channels. However, the system has several limitations as follows:

- Use VCO as the microwave source: A VCO is usually used for synthesizing high frequencies. The output frequency of VCO is linearly related to its input voltage. Its response is rapid, and it is suitable for sweep frequencies. However, it has 2 main disadvantages. First, the output frequency is directly determined by the input voltage. Any noise of the control voltage can contribute noises to the RF output. Second, a VCO usually has a narrow output bandwidth.
- No harmonic filters: The Harmonic effect is a common phenomenon in RF frequencies. That could be caused by many factors such as mismatch in transmission lines, imperfections of the

synthesizer and interference. And it is usually not possible to eliminate the harmonics from the source. The harmonics are typically reduced by adding multiband filters. Errors might occur if no harmonic filtering is used.

- Complicated and expensive control and DAQ system: National Instrument DAQ and control system and LabVIEW software are used in that research. That configuration is useful for evaluated a new idea, but it is not the best option for developing a usable product because the system is complex, bulky and expensive.
- No calibration algorithm: Though a gain & phase detector is used it that research, only gain data was measured. Errors due to the mismatch of the transmission line cannot be effectively reduced unless phase data is used to calibrate the measurement at each frequency.

Therefore, for new VNA design proposed in this research, several improvements are made. The VCO is changed to a PLL higher accuracy and reliability on output frequency. The harmonic filter is added to the system to inhibit harmonic effects. An Arduino microcontroller is used as the control and DAQ system to reduce the complexity and cost. Finally, a python program integrated with calibration algorithms is developed.

5.2 Design and Fabrication of the System

The microwave signal analyzer consists of 5 main subsystems, which are a PLL microwave synthesizer, a harmonic filtering module, a bi-directional coupler, a gain detector. The microwave signal path is connected through 50 Ω coaxial cables for impedance match. An Arduino microcontroller (MEGA2560) was applied to control the PLL microwave signal generation, control the pair of RF switches in the harmonic filtering module and to collect data from the gain detector. Frequency and raw gain data are synchronized by the microcontroller, and they were sent to PC for calibration and post data processing through Python scripts. A simplified schematic diagram of the system is shown in figure 5.1. The Arduino controller first sends a command to the PLL to synthesize a specific frequency. The raw output is then going through the harmonic filter module to screen out harmonic frequencies. The treated wave then goes to the signal-in port of the coupler and leaves from the signal-out port to the DUT. Forward and backward waves are coupled from the two coupling ports of the coupler and sent to the gain and phase detector. Magnitude and phase variations of the forward and backward waves are transformed to voltage data and sampled by the integrated analog to digital converter on Arduino controller. Finally, the frequency, magnitude and phase data are sent to the PC for post data processing by the Python code. Picture 5.2 shows the image of the customized VNA setup.

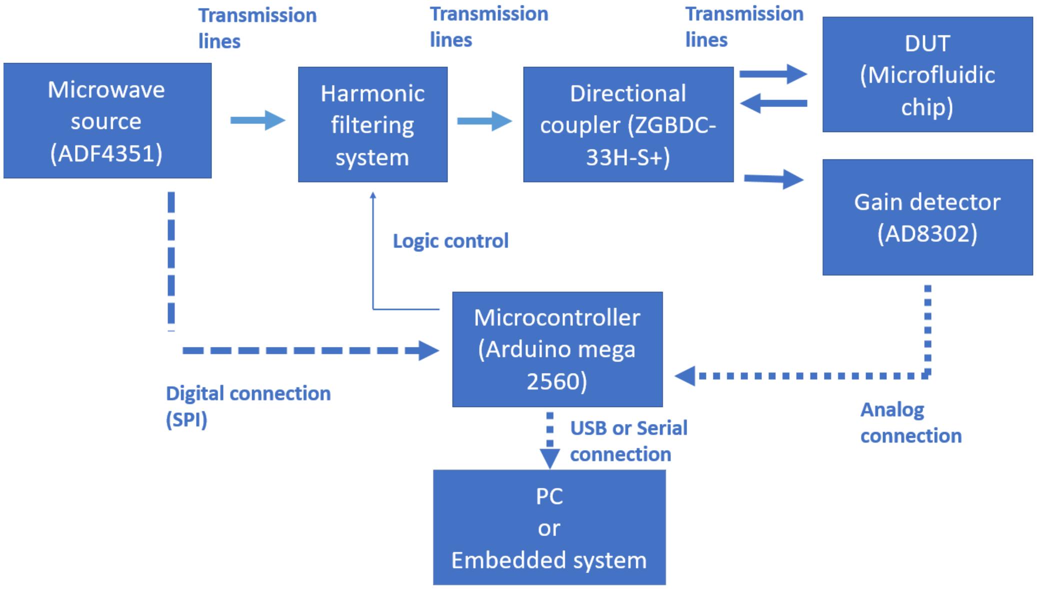

Figure 5-1 Schematic interpretation of the customized VNA.

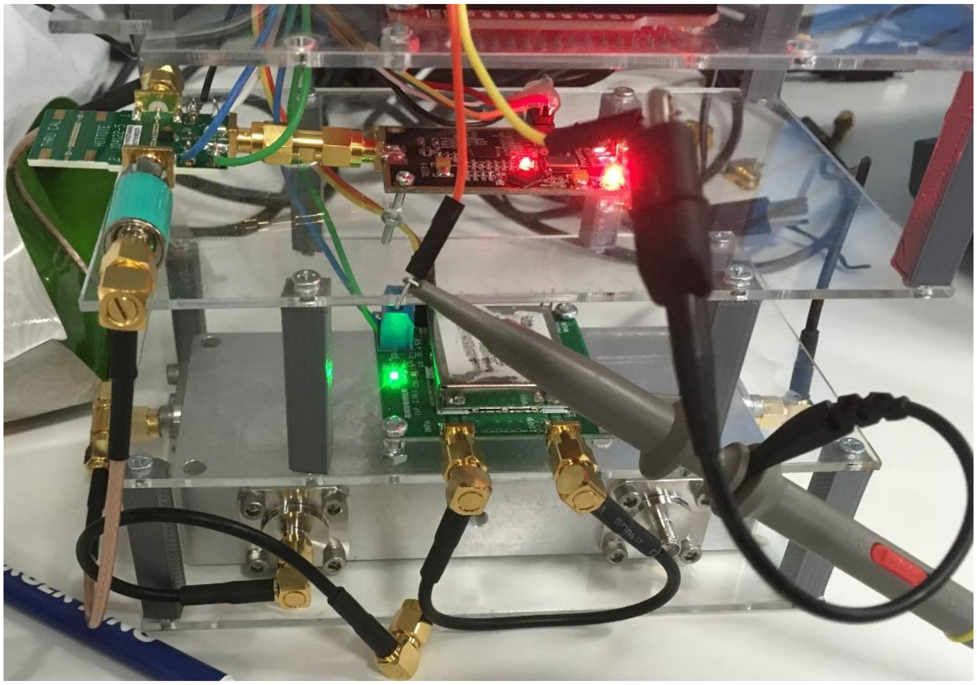

Figure 5-2 Picture of the customized VNA

5.2.1 PLL Microwave Synthesizer

A PLL synthesizer (Analog Devices, ADF4351) is used to provide the microwave signal source to the system. It has three integrated VCOs and frequency dividers so that it can generate a wide range of

RF signals from 35 to 4400 MHz. The output frequencies, output power, and other configurations are controlled through the SPI protocol. The Arduino controller sends new commands to update the outputs. In this experiment, the frequency range is set to 500 to 2700 MHz with 2000 linear frequency points, output power is 0 dBm, and frequency sweep speed is 15 ms per frequency point.

5.2.2 Harmonic Filter

Harmonics were observed from the raw output of the PLL which is shown at figure 5.3. The peak with the marker 2 is the target output frequency. The other peaks with frequencies that are integer multiple of the target frequency are the harmonic frequency. Those harmonics might influence the final measurements and need to be eliminated.

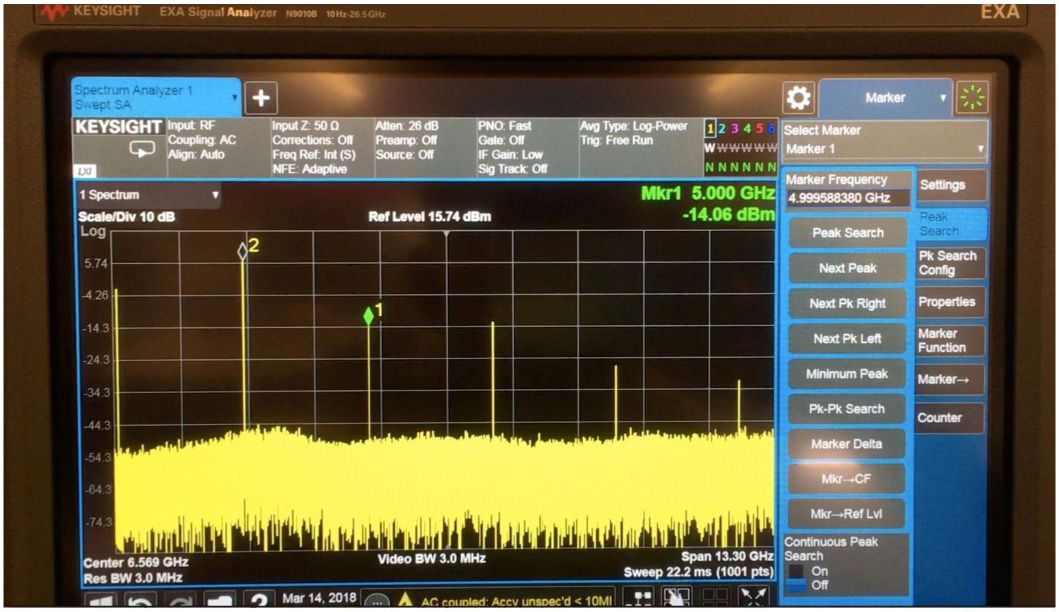

Input: RF
Coupling: AC
Align: Auto
Input Z: 50 Ω
Corrections: Off
Freq Ref: Int (S)
NFE: Adaptive
Atten: 26 dB
Preamp: Off
Source: Off
PNO: Fast
Gate: Off
IF Gain: Low
Sig Track: Off
Avg Type: Log-Power
Trig: Free Run
Select Marker: Marker 1
Marker Frequency: 4.999588380 GHz
Mkr1 5.000 GHz -14.06 dBm
Scale/Div 10 dB
Ref Level 15.74 dBm
Center 6.569 GHz
Res BW 3.0 MHz
Video BW 3.0 MHz
Span 13.30 GHz
Sweep 22.2 ms (1001 pts)
Mar 14, 2018
AC coupled: Accy unspec'd < 10MI

Figure 5-3 Spectrum measurement of raw output from the microwave source presenting the harmonic effects.

The harmonic filter in this research is built with a 1 GHz low pass filter (Crystek, CLPFL-1000) and 2 RF switches (brand, model). The RF switch has one input port and two output ports that can be controlled. The schematic and picture of the module are shown in figure 5.4. If the output frequency is from 500 to 1000 MHz, the harmonic frequencies will all be higher than 1 GHz. Thus, the wave is switched to the 1 GHz filter to screen out the harmonics. If the frequency is from 1000 to 2700 MHz, most of the harmonic frequency will be higher than 2700 MHz. The response of the detector used in this research is not sensitive over that frequency, so any output frequency between 1000 to 2700 MHz is switched to a coaxial line with no filter.

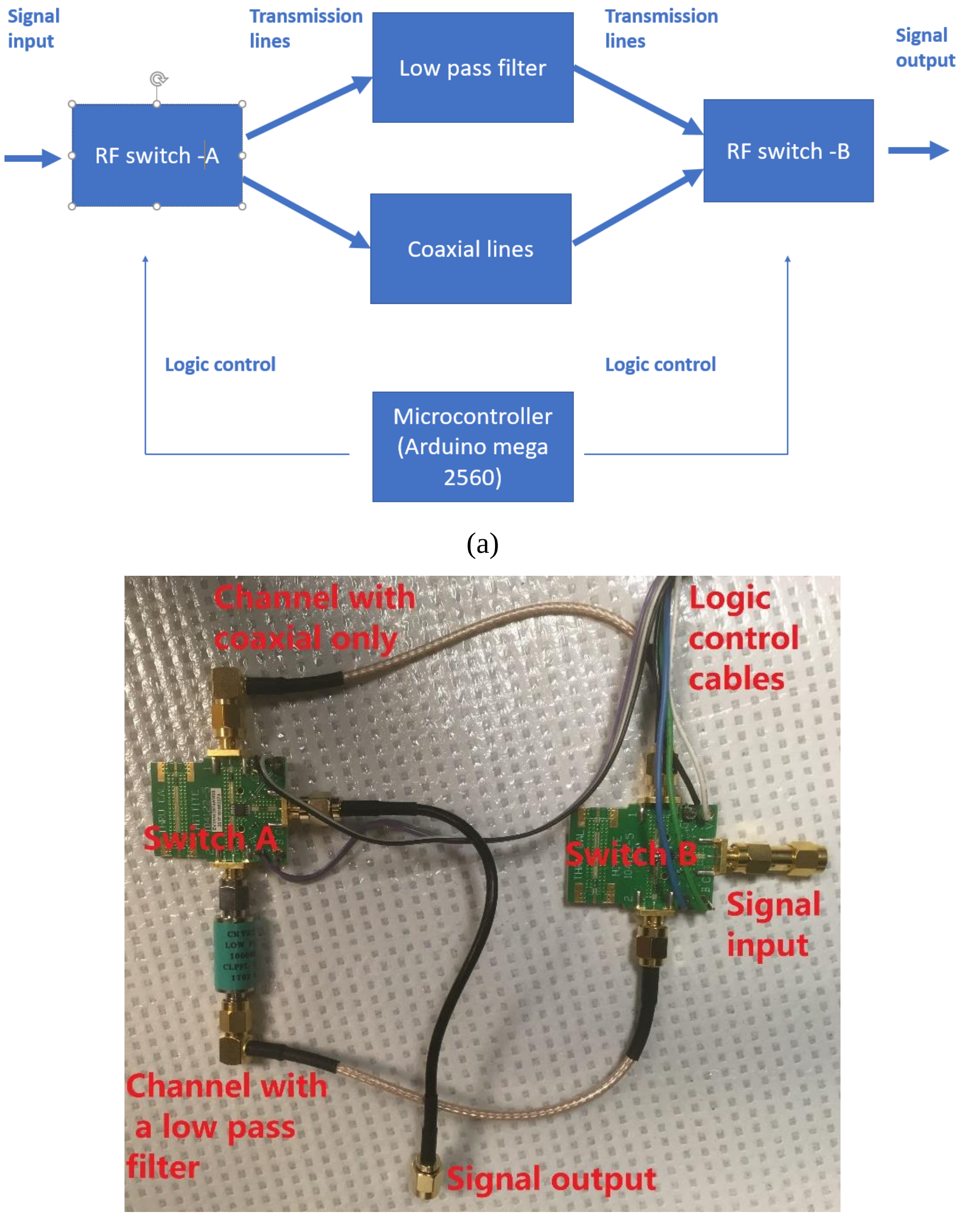

(a)

(b)

Figure 5-4 Schematic (a) and the picture (b) of the harmonic filter module.

5.2.3 Bidirectional Coupler

A plug-in-type bidirectional coupler (Mini-circuits, ZGBDC-33H-S+) is used to extract and separated the forward and backward waves from the transmission line. It has 4 SMA ports that are a signal-in port, a signal-out port, a forward coupling port, and a backward coupling port. Two signal ports are connected to the main transmission line. The reflection coefficient could be calculated by divide the power of backward port by the one from the forward port.

5.2.4 Gain and Phase Detector

The gain and phase detector (AD8302, Analog Devices) has 2 SMA input channel
It can transform the power and phase differences of the RF waves of the two input channels into DC voltages in linear relations. So, the reflection coefficient and phase delay could be calculated from the output voltages. Noises are observed from the detector, and they are reduced digitally by calculating the mean values from 10 repeat samplings.

5.2.5 Microcontroller

The Arduino microcontroller (Atmel, MEGA2560) has multiple roles, it acts as a central controller, a DAQ system, a simple raw data processor. It sends commands to the PLL through SPI to perform frequency sweep from 500 to 2700 MHz. It also controls 2 RF switches by digital outputs. Two 10-bit integrated ADCs are used to measure the output voltages from the gain detector. Frequency, gain and phase data are synchronized, and they are sent to PC by the serial protocol for data saving, post processing, and interpretation. All functions are programmed in C++ code.

5.3 Python program for data manipulation and calibration algorithm

A python program on PC handles the communications with the Arduino controller. The program has three main functions which are receiving real-time measuring results from the controller, post-processing data with calibration algorithm, organizing the data and save them to CSV files.
The calibration algorithm applies the 3-error model and SOL calibration method, which were discussed in chapter 2, to reduce the noises that caused by the standing waves.

5.4 Evaluation of the New Customized Circuitry

The performance of the customized VNA is evaluated by comparing with a commercial VNA. Both devices are calibrated with the same SOL calibration kit. Figure 5.5 interprets the measurement results from the devices. It can be observed that the un-calibrated result has multiple peak and ripples on the spectrum which are caused by the standing waves in transmission lines and directivity errors in the directional coupler. The calibration reduces those errors. Therefore, the spectrum of calibrated result has a more similar pattern than the un-calibrated with commercial VNA that is used as the reference. However, the peak frequency result reveals that there is still variance between the customized VNA and commercial VNA (table 5.1).

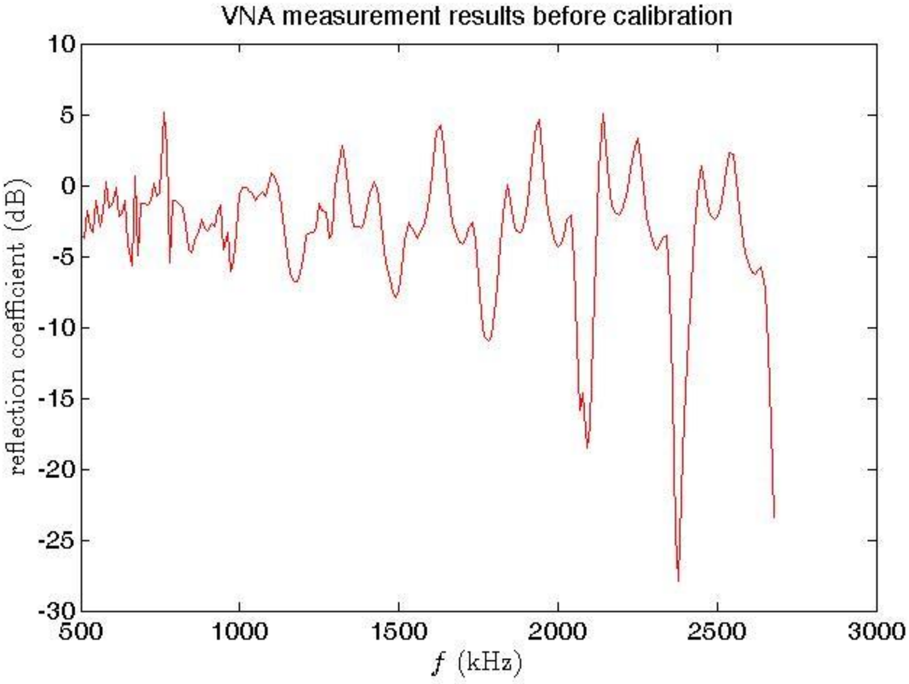

(a)

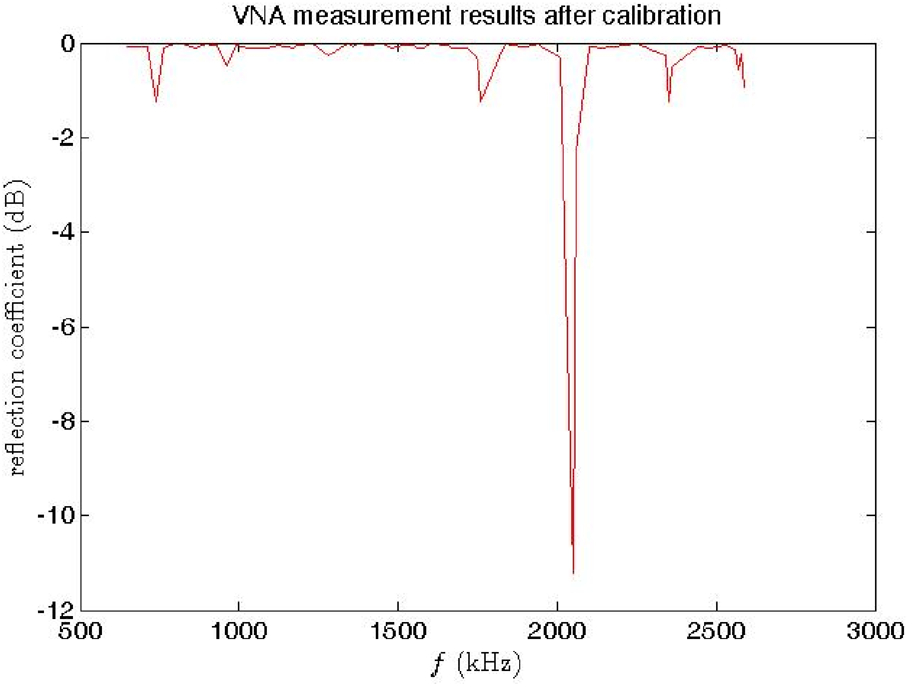

(b)

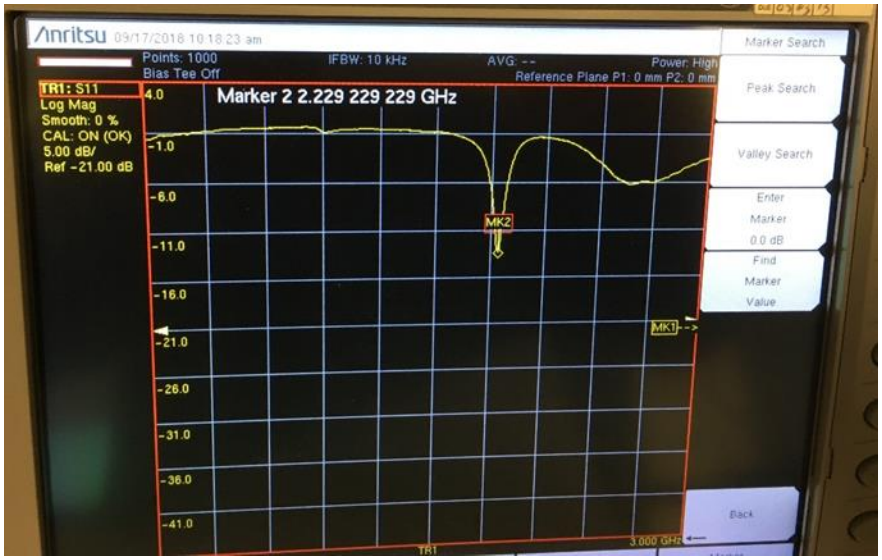

(c)

Figure 5.5: Measurement results of a random sensor: a- un-calibrated results from the customized VNA, b- calibrated data with SOL method, c- measurement result from the calibrated commercial VNA

Table 5.1: Peak frequencies from un-calibrated customized VNA, customized VNA, and commercial VNA

	The un-calibrated result from customized VNA	The calibrated result from customized VNA	Results from the commercial VNA
Peak frequency (GHz)	2.4	2.05	2.2
Relative error	+9%	-6.8%	

Chapter 6 Contributions

This chapter gives a summary of the work that has been implemented in this research, which includes the contributions of the thesis and the recommendations for further study.

6.1 The Contribution of This Research

Microfluidics combining with the on-chip sensing techniques are a promising technology with great potentials on nanobiotechnology, material science, and medicine, because of its unique benefits of lower consumption of the reagents, lower costs, high sensitivity, better control of the reaction and incredibly miniaturized size. The conventional microfluidic systems have been well developed, but the on-chip sensing techniques are still in their infancy and efforts should be continued for the development of a compact, cost-effective, sensitive, reproducible sensing and detection technologies. However, most microfluidic sensing platforms use optical and electrical method for sensing. They are either complicated, bulky, expensive or less sensitive.

Microwave sensing is becoming a promising technology for the characterization of fluids in the microfluidic channel. There are changelings of transforming the previous designs of the sensor into the practical applications. For two ports sensors, the overall cost could not be reduced because the price of a dual-port VNA is much higher than the single-port one. For glass-based sensors, their high material costs and complicated fabrication processes also limit their progress from academic research to industries. Therefore, a new design of the SRR sensor, more straightforward fabrication approach and easier measuring operations of the system were proposed, developed and interpreted in this thesis.

As part of the objects of this thesis, a PCB-based SRR sensor was successfully developed. The substrate of the sensor was changed from glass to FR-4 for lower material cost and easier fabrication. The copper trace was fabricated by photolithography from an industrial manufactory, where a 10 υμ thick passivation was also sprayed onto the board. The size of the sensor needs to be optimized due to the material change. The response of the single port SRR was analyzed by considering it as a series RLC circuit. Numerical expressions of the sensor's resonant frequency as the function of its geometry were derived. The SRR design was also evaluated by the HFSS and measurements of the real sensor with VNA. The measurement result of the SSR did not match perfectly with the calculated and simulated results, which is probably due to the improper molding of the structure.

Two measuring methods using the newly developed PCB sensors were also implemented, with one that was directly dipped into the liquid and the other one combined with a tape channel. Both systems were capable of discrimination of pure liquids and mixtures at different solute fractions. The results also revealed that the dip-mode sensor had a greater shift of peaks and more information on the spectrum (two moving peaks) than the tape-channel-mode, but it has lower reproducibility and more complex operations for performing the tests. The dip-mode is better for qualitative measurements such as monitoring fixed contents, whereas the tape-channel mode is more suitable for quantitative analysis because of its better linear response. Errors and uncertainties were discussed for both approaches, and improvements should be done in further work to optimize the sensor's performance.
A fully-customized VNA circuit solution was proposed and implemented in this research as an improvement of the previous work, with modifications of the microwave source, the addition of the harmonic filtering system, the changing to fully-customized control and DAQ platform and the development of the data post processing and calibration algorithms. The system was built from multiple RF modules, and it was also evaluated with the real sensor. The measurement of a SRR sensor from the customized VNA has a comparable patter as the commercial VNA.
However, the peak frequencies are not matched perfectly. Therefore, a number of works require to be done on further research for improving the prediction accuracy.

6.2 Future Works and Recommendations

This thesis is an initial stage of transferring the proof of concept further into the practical applications. The next step of the design will focus on the modifications of the numerical expressions of the SRR’s resonant frequencies for more accurate predictions, improvements on sensor design for lower noise levels, and improvements on customized VNA design for better performance. Those improvements for the future works are described as followings.

6.2.1 Modifications of Numerical Expressions and Simulations

The results derived from the numerical expressions and the HFSS simulations are not well matched with the experimental measurement results. For the numerical expression, the equations used for calculating the capacitance and inductance should be modified for a more accurate resonant frequency prediction of a SRR. That could be achieved by measuring various sensors of different designs and using the results to modify the numerical expressions. For the numerical simulation, the double-ring structure should be created in the HFSS to simulate the reflections instead of the transmissions.

6.2.2 Improvement of Chip Design

There are 2 main improvements need to be done for the chip design. First, only resonant frequency of the SRR is optimized during the design. However, the effects of the geometrical parameters on the sensor’s performance are not clear. More studies require to be conducted in the further study to investigate those effects for optimizing the sensor. Second, proper shielding protections should be added to protect the sensor from the outsource interferences, to increase the SNR.

6.2.3 Improvement of the VNA Circuitry

For the VNA circuitry, all the major components should be integrated in the next version because the standing-wave interferences can be decreased if the length of the transmission lines is much smaller than the wave length of the microwaves. There is also a need for exploring a more precise and lower-noise phase & gain detector to increase the stability of the measurements.

Bibliography

Abduljabar, A. A., Rowe, D. J., Porch, A., & Barrow, D. A. (2014). Novel microwave microfluidic sensor using a microstrip split-ring resonator. *IEEE Transactions on Microwave Theory and Techniques*, *62*(3), 679–688. https://doi.org/10.1109/TMTT.2014.2300066

Boybay, M. S., Jiao, A., Glawdel, T., & Ren, C. L. (2013). Microwave sensing and heating of individual droplets in microfluidic devices. *Lab on a Chip*, *13*(19), 3840–3846. https://doi.org/10.1039/c3lc50418b

Camli, B., Kusakci, E., Lafci, B., Salman, S., Torun, H., & Yalcinkaya, A. (2016). A Microwave Ring Resonator Based Glucose Sensor. *Procedia Engineering*, *168*, 465–468. https://doi.org/10.1016/j.proeng.2016.11.127

Chahadih, A., Cresson, P. Y., Hamouda, Z., Gu, S., Mismer, C., & Lasri, T. (2015). Microwave/microfluidic sensor fabricated on a flexible kapton substrate for complex permittivity characterization of liquids. *Sensors and Actuators, A: Physical*, *229*, 128–135. https://doi.org/10.1016/j.sna.2015.03.027

Chow, A. W. (2002). Lab-on-a-chip: Opportunities for chemical engineering. *AIChE Journal*, *48*(8), 1590–1595. https://doi.org/10.1002/aic.690480802

Chretiennot, T., Dubuc, D., & Grenier, K. (2016). Microwave-based microfluidic sensor for non-destructive and quantitative glucose monitoring in aqueous solution. *Sensors (Switzerland)*, *16*(10). https://doi.org/10.3390/s16101733

Curtis, T. M., Widder, M. W., Brennan, L. M., Schwager, S. J., Van Der Schalie, W. H., Fey, J., & Salazar, N. (2009). A portable cell-based impedance sensor for toxicity testing of drinking water. *Lab on a Chip*, *9*(15), 2176–2183. https://doi.org/10.1039/b901314h

Demori, M., Ferrari, V., Poesio, P., & Strazza, D. (2011). A microfluidic capacitance sensor for fluid discrimination and characterization. *Sensors and Actuators, A: Physical*, *172*(1), 212–219. https://doi.org/10.1016/j.sna.2011.07.013

Dong, T., & Barbosa, C. (2015). Capacitance variation induced by microfluidic two-phase flow across insulated interdigital electrodes in lab-on-chip devices. *Sensors (Switzerland)*, *15*(2), 2694–2708. https://doi.org/10.3390/s150202694

Grover, F. W. (1962). *Inductance Calculations: Working Formulas and Tabels.* Instrument Society of America. https://doi.org/10.1038/163195a0

Harnsoongnoen, S., & Wanthong, A. (2017). Real-time monitoring of sucrose, sorbitol, D-glucose and D-fructose concentration by electromagnetic sensing. *Food Chemistry, 232*, 566–570. https://doi.org/10.1016/j.foodchem.2017.04.054

Jabita, & Abiodun, A.-N. (2013). Design of Singly Split Single Ring Resonator for Measurement of Dielectric Constant of Materials using Resonant Method. *Master's Thesis in Electronics and Telecommunications, Univ. Gävle*, (June).

Kozlov, M., & Turner, R. (2010). A comparison of Ansoft HFSS and CST Microwave Studio Simulation Software for Multi-channel Coil Design and SAR Estimation at 7T MRI. *PIERS Online*, *6*(4), 395–399. https://doi.org/10.2529/PIERS090902092851

Li, X. B., Larson, S. D., Zyuzin, A. S., & Mamishev, A. V. (2006). Design principles for multicuhannel fringing electric field sensors. *IEEE Sensors Journal*, *6*(2), 434–440. https://doi.org/10.1109/JSEN.2006.870161

Martinez, M. (2012). Design and implementation of a compact Vector Network Analyzer.

Mcdermott, B. T., & Ireland, K. (2004). A Low-Cost 100 MHz Vector Network Analyzer with USB Interface, 3–14.

Medoro, G., Guerrieri, R., Manaresi, N., Nastruzzi, C., & Gambari, R. (2007). Lab on a chip for live-cell manipulation. *IEEE Design and Test of Computers*, *24*(1), 26–36. https://doi.org/10.1109/MDT.2007.21

Medoro, G., Manaresi, N., Leonardi, A., Altomare, L., Tartagni, M., & Guerrieri, R. (2003). A lab-on-a-chip for cell detection and manipulation. *IEEE Sensors Journal*, *3*(3), 317–325. https://doi.org/10.1109/JSEN.2003.814648

Nikolic-Jaric, M., Romanuik, S. F., Ferrier, G. A., Bridges, G. E., Butler, M., Sunley, K., … Freeman, M. R. (2009). Microwave frequency sensor for detection of biological cells in microfluidic channels. *Biomicrofluidics, 3*(3), 1–15. https://doi.org/10.1063/1.3187149

Pozar, D. M. (2012). Microwave Engineering. *Wiley*. https://doi.org/10.1080/01422419908228843

Rytting, D. (1998). *Network Analyzer Error Models and by*. *White Paper September*. Retrieved from http://www-ee.uta.edu/online/adavis/ee5349/NA_Error_Models_and_Cal_Methods.pdf

Sydoruk, O., Tatartschuk, E., Shamonina, E., & Solymar, L. (2009). Analytical formulation for the resonant frequency of split rings. *Journal of Applied Physics*, *105*(1), 1–5. https://doi.org/10.1063/1.3056052

Toepke, M. W., & Beebe, D. J. (2006). PDMS absorption of small molecules and consequences in microfluidic applications. *Lab on a Chip*, *6*(12), 1484–1486. https://doi.org/10.1039/b612140c

Vélez, P., Su, L., Grenier, K., Dubuc, D., & Martín, F. (2017). Microwave Microfluidic Sensor based on a Microstrip Splitter / Combiner Configuration and Split Ring Resonators (SRR) for Dielectric Characterization of Liquids. *IEEE Sensors Journal, Institute of Electrical and Electronics Engineers*, *1748*(c), 1–10. https://doi.org/10.1109/JSEN.2017.2747764

Wong, D., Yesiloz, G., Boybay, M. S., & Ren, C. L. (2016). Microwave temperature measurement in microfluidic devices. *Lab on a Chip*, *16*(12), 2192–2197. https://doi.org/10.1039/c6lc00260a

Wu, J., & Gu, M. (2011). Microfluidic sensing: state of the art fabrication and detection techniques. *Journal of Biomedical Optics*, *16*(8), 080901. https://doi.org/10.1117/1.3607430

Yesiloz, G., Boybay, M. S., & Ren, C. L. (2015). Label-free high-throughput detection and content sensing of individual droplets in microfluidic systems. *Lab on a Chip*, *15*(20), 4008–4019. https://doi.org/10.1039/c5lc00314h

Zarifi, M. H., Farsinezhad, S., Abdolrazzaghi, M., Daneshmand, M., & Shankar, K. (2016). Selective microwave sensors exploiting the interaction of analytes with trap states in TiO2nanotube arrays. *Nanoscale*, *8*(14), 7466–7473. https://doi.org/10.1039/c5nr06567d

Zarifi, M. H., Rahimi, M., Daneshmand, M., & Thundat, T. (2015). Microwave ring resonator-based non-contact interface sensor for oil sands applications. *Sensors and Actuators, B: Chemical*, *224*, 632–639. https://doi.org/10.1016/j.snb.2015.10.061

Appendix A

The Python Code Example for Automatic Extraction of Peak Info

```
def peakdect(x,y,delta):
    maxtab = []
    mintab = []

    x_mn, x_mx = np.NAN, np.NAN
    y_mn, y_mx = np.inf, -np.inf

    x_len = len(x)
    y_len = len(y)
    if x_len != y_len:
        print('error(peakdect): x,y len not match')
    look_for_max = True

    for i in range(x_len):
        this = float(y[i])
        idx = float(x[i])
        if this > y_mx:
            y_mx = this
            x_mx = idx
        if this < y_mn:
            y_mn = this
            x_mn = idx

        if look_for_max:
            if this < y_mx - delta:
                maxtab.append([x_mx,y_mx])
                y_mn = this
                look_for_max = False
        else:
            if this > y_mn + delta:
                mintab.append([x_mn,y_mn])
                y_mx = this
                look_for_max = True

    return mintab
```